Space Science Reviews (2025) 221:105
https://doi.org/10.1007/s11214-025-01233-y

GLObal Solar Wind Structure (GLOWS)

Maciej Bzowski[1] · Roman Wawrzaszek[1] · Marek Strumik[1] · Jędrzej Baran[1] · Tomasz Barciński[1] · Kamil Ber[1,2] · Waldemar Bujwan[1] · Maciej Daukszo[1] · Kamil Jasiński[1] · Grzegorz Juchnikowski[1] · Przemyslaw Kazmierczak[1] · Izabela Kowalska-Leszczyńska[1] · Tomasz Kowalski[1] · Marzena Kubiak[1] · Jakub Mądry[1] · Aleksandra Mirońska[1] · Karol Mostowy[1] · Piotr Orleański[1] · Czesław Porowski[1] · Jakub Półtorak[1] · Tomasz Rajkowski[1] · Joanna Rothkaehl[1] · Tomasz Rudnicki[1] · Aliaksandra Shmyk[1] · Adam Sikorski[1] · Michał Turek[1] · Marek Winkler[1] · Katarzyna Wojciechowska[1] · Tomasz Zawistowski[1] · Hans J. Fahr[3] · Uwe Nass[3] · Piotr Osica[4] · Karolina Wielgos[4] · Alexander Gottwald[5] · Hendrik Kaser[5] · Mark Krzyzagorski[5] · Marek Antoniak[6] · Marcin Drobik[6] · Grzegorz Gajoch[6] · Tomasz Martyniak[6] · Rafał Żogała[6] · Andrzej Bartnik[7] · Henryk Fiedorowicz[7] · Tomasz Fok[7] · Mateusz Majszyk[7] · Przemysław Wachulak[7] · Martyna Wardzińska[7] · Łukasz Węgrzyński[7] · Robert Kosturek[8] · Carlos Urdiales[9] · Mark Tapley[9] · Susan Pope[9] · Daniel B. Reisenfeld[10] · Matina Gkioulidou[11] · Nathan A. Schwadron[12] · Eric R. Christian[13] · David J. McComas[14]

Received: 10 July 2025 / Accepted: 15 October 2025

Abstract

Information on the evolution of latitudinal profiles of the solar wind speed and density is one of the important elements needed to understand global observations of heliospheric neutral and charged particle populations performed by NASA's integrated heliospheric observatory Interstellar Mapping and Acceleration Probe (IMAP). This information is provided by the GLObal solar Wind Structure (GLOWS) experiment. GLOWS is a single-pixel Lyman-α photometer that observes the heliospheric backscatter glow emitted by interstellar neutral (ISN) H inside the heliosphere, illuminated by the solar Lyman-α emission. GLOWS features a specially designed optical entrance system with a baffle, collimator, and interference filter; a channeltron-based photon event detector; a digital processing unit (DPU) with custom-designed software that registers photon events and assembles lightcurves; a front-end electronics block that interfaces the detector and DPU; and the necessary power and voltage distribution system. Due to charge-exchange between ISN H and the solar wind, the helioglow bears imprints of the solar wind structure. Analysis of lightcurves observed daily along Sun-centered circles with a 75° radius in the sky yields profiles of intensities of the charge exchange reaction, which are decomposed into solar wind speed and density profiles at a Carrington period cadence. With them, it is possible to infer the shape of the heliosphere and its variation during the solar cycle and to determine the attenuation through re-ionization of energetic neutral atom fluxes between the ENA creation sites in the inner heliosheath and the IMAP ENA detectors.

Extended author information available on the last page of the article

1 Introduction

GLOWS (GLObal solar Wind Structure) is one of the experiments on the NASA Interstellar Mapping and Acceleration Probe (IMAP) mission (McComas et al. 2025, this journal). The objective of GLOWS is to investigate the global heliolatitudinal structure of the solar wind and its evolution over the solar activity cycle. Additionally, GLOWS investigates the distribution of interstellar neutral hydrogen (ISN H) inside the heliosphere and the solar radiation pressure acting on ISN H.

The objectives of GLOWS are accomplished by observations of the heliospheric hydrogen backscatter glow, or "helioglow". The helioglow is created by resonant excitation of ISN H atoms within several au from the Sun by the intense solar electromagnetic radiation in the Lyman-α waveband 121.567 nm (see reviews by Fahr 1974; Baliukin et al. 2022). The ISN H gas in this region is collisionless, and thus immediately after an atom is excited by a photon, it re-emits another photon in a random direction at an almost identical wavelength (for details, see, e.g., Brasken and Kyrola 1998). Collectively, the re-emitted photons form the helioglow. The intensity of the helioglow varies across the sky from $\sim 200 - 1500$ Rayleigh (Quémerais et al. 2013).

The density and velocity of ISN H gas inside the heliosphere are governed by solar gravity and radiation pressure in the Lyman-α line on one hand, and by ionization losses on the other hand (Bzowski et al. 1997). If the solar emissions were spherically symmetric, the flow pattern of ISN H would be axially symmetric with the symmetry axis coincident with the inflow direction. The distribution of the helioglow across the sky, when viewed from the Sun's center, would feature a characteristic pattern organized around the upwind–downwind axis, with details depending on the Mach number of the flow, magnitude of radiation pressure, and intensity of ionization losses. This pattern is modified by the parallax effect when viewed from vantage points offset from the Sun's center. The parallax effect in the helioglow sky distribution can be identified by comparison of the sky maps simulated for the upwind and crosswind vantage points, as illustrated in Fig. 1.

The processes of ionization of ISN H include (1) charge exchange between H atoms and charged particles forming the solar wind (mostly protons and alpha particles), (2) photoionization by solar radiation with the wavelengths shorter than the threshold for H ionization at ~ 91.2 nm, and, (3) within 1–2 au from the Sun, by solar wind electron impact (Bzowski et al. 2013).

The solar wind has a latitudinal structure that evolves over the solar activity cycle. This removes the spherical symmetry of the ionization rate, which results in a removal of the axial symmetry of the density distribution of ISN H and consequently of the sky distribution of the helioglow viewed from Sun's center.

Thus, by observing the sky distribution of the helioglow and taking appropriately into account the off-center viewing geometry, it is possible to infer the latitudinal structure of the solar wind. Further, by monitoring the helioglow between the minimum and maximum of solar activity, it is possible to monitor the evolution of the global solar wind structure. Performing this study was proposed by Lallement et al. (1995), and implemented in full-sky survey of the helioglow within the SWAN experiment (Bertaux et al. 1995) onboard the ESA mission Solar and Heliospheric Observatory (SOHO). Analysis of full-sky maps produced a line of papers deriving the solar wind structure (e.g., Lallement et al. (2010), Katushkina et al. (2013), Koutroumpa et al. (2019), see Baliukin et al. (2022) for a recent review). Bzowski (2003) pointed out that the solar wind structure can be obtained from a limited set of observations of the helioglow in the form of lightcurves from Sun-centered circles in the sky, and Bzowski et al. (2003) successfully implemented this method in analysis of SWAN observations from 1996–2002.

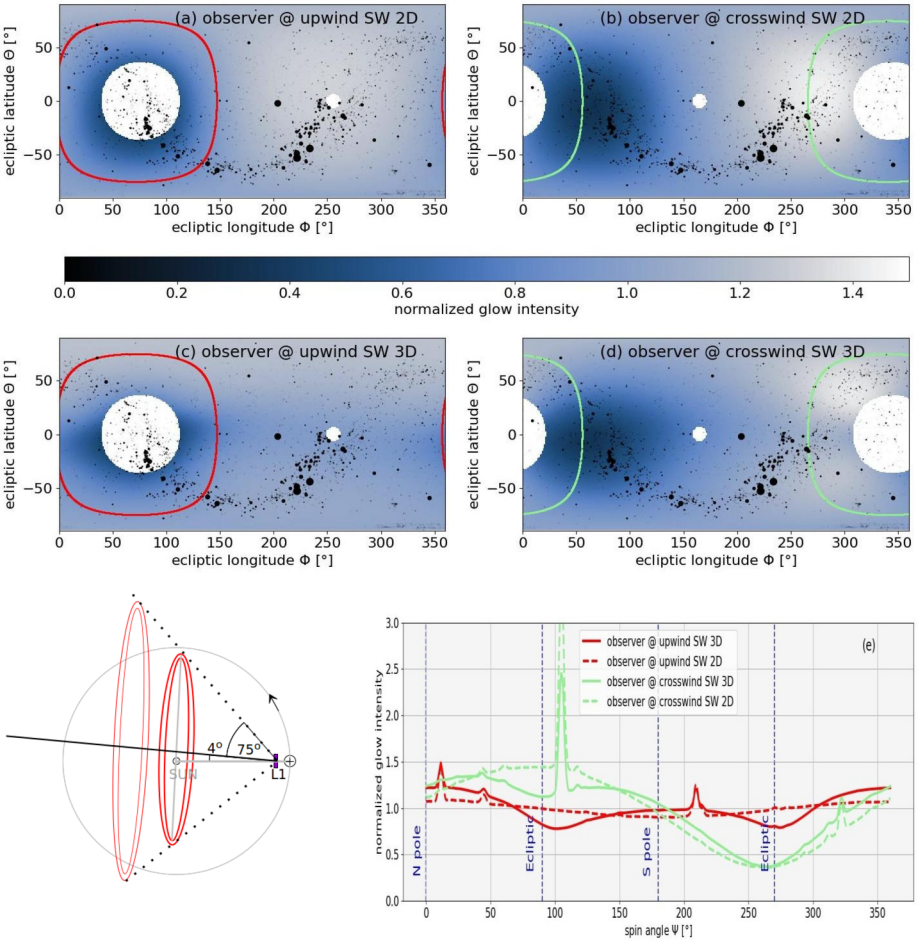

Fig. 1 Color-coded sky maps of the helioglow for an observer located at the upwind (left) or crosswind (right) vantage points at 1 au, simulated for two models of latitudinal distribution of the ionization rate of ISN H: spherically symmetric (upper row) and latitudinally structured (middle row). The darkening of the helioglow in an equatorial band, clearly visible in the second row of helioglow maps, is due to an increased ionization in an equatorial latitudinal band (Porowski et al. 2023). Dots mark stars visible in the GLOWS waveband. The lower-left panel presents the observation geometry viewed from above the ecliptic plane, with IMAP (purple) sitting at L1 inside the Earth orbit, and GLOWS scanning a 75° circle in the sky (red) centered 4° off the Sun. The scanning circle is represented by red and green circles in the sky maps. The lower right panel presents the lightcurves for the scanning circles shown in the maps. The maps and the lightcurves are normalized to the mean values for the individual lightcurves. GLOWS seeks to interpret departures of the actually observed lightcurves, expected to be similar to those drawn with solid lines, from those characteristic for spherically symmetric ionization rates, presented in the lower panel with broken lines. Note the spikes in the lightcurves due to EUV-bright stars traversing the instrument FoV during scanning

Analysis of latitudinal anisotropy of the solar wind was also performed by Hord et al. (1991), Pryor et al. (1992, 1996), and Pryor et al. (2003) based on observations from the EUVS experiment onboard Cassini (Hord et al. 1992). These authors pointed out the significance of the longitudinal and latitudinal anisotropy of the solar Lyman-α output in the helioglow analysis. The longitudinal anisotropy, also known as the searchlight effect, was

signaled by Bertaux et al. (2000). The latitudinal anisotropy features variations during the solar activity cycle was analyzed for various epochs during the solar activity cycle by Strumik et al. (2021, 2024a).

GLOWS implements the ideas put forward by Bzowski (2003) in a dedicated experiment. GLOWS scans the sky along a narrow ring ("a scanning circle") with a radius of 75° centered at the IMAP rotation axis. Thus, the scanning circle is located within the solar hemisphere. Effectively, GLOWS produces daily lightcurves that collect light within a narrow band around the Lyman-α wavelength. The IMAP rotation axis is shifted approximately 1° every day to maintain it along the average aberrated solar wind direction by pointing it $\sim 4°$ off the Sun's center. This results in an equivalent shift of the scanning circle in the sky, but its position relative to the Sun is maintained.

Example sky maps with the superimposed GLOWS scanning circle, and the corresponding lightcurves and profiles of the ionization rate of ISN H are shown in Fig. 1.

2 Science Requirements and Capabilities

2.1 Scientific Objectives

The objective of the GLOWS experiment is to retrieve latitudinal profiles of the solar wind speed and density at 1 au from the Sun at a cadence comparable to the travel time of typical heliospheric ENAs from the solar wind termination shock to 1 au and investigate their evolution over the solar cycle. Based on these profiles, attenuation factors of heliospheric ENAs inside the termination shock are also obtained.

Monitoring the latitudinal structure of solar wind is needed to better understand the solar activity, but also for interpretation of observations by other IMAP experiments, in particular those observing ENAs and ISN gas. Neutral atoms inside the heliosphere are subjected to ionization losses, which attenuate the ENA and ISN fluxes observed at 1 au (Bzowski 2008). The main loss reaction is charge exchange of H atoms with solar wind protons p

$$\mathrm{H} + \mathrm{p} \rightarrow \mathrm{H}^{+}_{\mathrm{PUI}} + \mathrm{H}_{\mathrm{ENA}}. \tag{1}$$

This reaction is a source of two new populations of particles in the heliosphere, namely ENAs ($\mathrm{H}_{\mathrm{ENA}}$) and pickup protons ($\mathrm{H}^{+}_{\mathrm{PUI}}$).

Most of $\mathrm{H}_{\mathrm{ENA}}$ created inside the termination shock exit the heliosphere. Due to charge exchange and elastic collisions with atoms and ions of interstellar matter, they heat the immediate neighborhood around the heliosphere and, importantly, after re-ionization become the seed population in the secondary ENA production mechanism (McComas et al. 2009b; Heerikhuisen et al. 2010). Some of these secondary ENAs are observed by IMAP as Ribbon and obviously, they are closely related to the fast/slow solar wind (McComas et al. 2012, 2017).

Pickup ions (PUIs) are carried with the solar wind, and within the heliosheath are the main source of thermal pressure. They are also the source population for heliospheric ENAs (Gruntman et al. 2001), the so-called globally-distributed flux (GDF), observed by IMAP instruments (McComas et al. 2009c). Both Ribbon and GDF ENAs are subjected to re-ionization inside the termination shock before they reach IMAP detectors. Since the dominant reaction responsible for these losses is charge exchange with solar wind protons, and the rate of this reaction obviously depends on the density of the protons and the collision speed, measurements of the solar wind density and speed profiles during the mission are

needed to correctly account for losses in the interstellar atom and ENA fluxes between their origin in the boundary region of the heliosphere and the detection by IMAP.

The solar wind speed and density profiles from GLOWS become part of the WawHelioIon model of the ionization factors in the heliosphere (Bzowski et al. 2013; Sokół et al. 2013; Porowski et al. 2022). This model uses heliolatitudinal profiles of solar wind speed and density at a cadence of one Carrington rotation (CR) period and is used in modeling of ISN gas distribution inside the heliosphere. The WTPM model (Tarnopolski and Bzowski 2009; Sokół et al. 2015) is needed for interpretation of IMAP-Lo measurements of the ISN gas, in simulations of the helioglow with the WawHelioGlow code (Kubiak et al. 2021b), and in the calculation of survival probabilities of heliospheric ENAs (Bzowski 2008) used in the construction of ENA maps from IMAP Lo, IMAP Hi, and IMAP Ultra data (Reisenfeld 2025).

Variations of latitudinal profiles of the solar wind speed are used in the analysis of the size of the heliosphere based on measurements of the time difference between a change in the wind and the related change in the observed ENA flux (Reisenfeld et al. 2016, 2019, 2021). Thus, GLOWS needs to provide these profiles preferably at a cadence comparable to the typical travel times of the most energetic heliospheric ENAs from the termination shock, where their production ceases, and 1 au. These travels times for Ultra ENAs can be as low as ~ 27 days, i.e., close to the Carrington rotation period.

2.2 Sources of the Signal for GLOWS

The sources of the signal observed by GLOWS include:

1. *The heliospheric backscatter glow* in the Lyman-α line. The intensity varies from $\sim$ 200 to $\sim$ 1500 Rayleigh (Bertaux et al. 1996), and its spectral width $\simeq 0.012$ nm is extremely narrow in comparison with the other observed emissions. The wavelength of the line center varies within a similar range depending on the observation direction due to the Doppler effect because of the orbital motion of the spacecraft. The angular scale of important helioglow features is $>\sim 20°$ (see the second row of panels in Fig. 1). The helioglow evolves slowly during the solar activity cycle, and the observed signal changes gradually from day to day because of the spacecraft motion around the Sun and the related change in the spin axis of the spacecraft.
2. *Searchlights*, i.e., reflections of flares and active regions at the rotating Sun's surface off the interplanetary hydrogen. This effect is visible in global sky maps similarly to a searchlight beam reflected off clouds. A typical angular dimension of these brightening regions in the sky is on the order of $\sim 90°$ (Bertaux et al. 2000; Quémerais and Bertaux 2002a), and its magnitude varies by $\sim 10\%$ during the time of solar rotation (27.4 days).
3. *Extraheliospheric (EH) and Solar System sources*, i.e., stars, the Milky Way, comets, planets (Jupiter, Saturn, and Mars), the Moon and the Earth exosphere, etc. The stellar and Galactic components make a fixed-pattern background during a given observation day. The stars are point sources, but those within the width of the instrument point-spread function ($\sim 4°$) from each other are blended. The stars much dimmer than the helioglow cannot be resolved in the lightcurves but contribute to the observed signal. The intensity of this component is the largest in the Galactic plane and drops towards the Galactic poles (Strumik et al. 2020). The Moon is not visible during science operations but may be visible during the cruise phase shortly after launch. Due to the geometry of observations, the exosphere, which extends up to 100 radii around Earth (Baliukin et al. 2019), may be visible for some time during the IMAP cruise to L1, but not during regular science operations.

4. *Stray light from strong radiation sources*. Stray light is a component of the signal originating outside of the desired Field of View (FoV) and must be suppressed. The strongest source of this light is the Sun; additional sources are EUV-bright stars passing near the FoV and potentially light reflected off spacecraft components.
5. *Particle backgrounds*. This is the signal due to penetrating radiation (γ rays, electrons with energies > 10 MeV, ions with energies > 100 MeV, energetic neutrons; Funsten et al. 2015), solar energetic particles, cosmic rays, Earth bow shock particles (Wurz et al. 2021), and potentially due to solar wind electrons that are able to sneak inside the detector and hit the active surface of the channeltron. Funsten et al. (2015) suggested that the quantum efficiency of a channeltron detector for 663 keV γ-rays is 1.75×10^{-3}, largely independent of the detector bias. This component is most likely quite bursty, but its intensity can only be investigated after launch. It is not expected to be time-correlated with the remaining signal components in any way. Within the burst signal, the statistics is expected to be Poissonian. The arrival times of the bursts are expected to be random, but possibly correlated with solar cycle phase. Since IMAP measures both solar wind electrons (Skoug et al. 2025, this journal) and high-energy particle radiation (Christian et al. 2025, this journal), investigation of correlations between the GLOWS signal on one hand and solar wind electron and cosmic-ray fluxes on the other hand, observed after launch will help identify and subtract this component.
6. *Dark current due to the channeltron and electronics*. Based on ground measurements, this component is expected at a level of $0.5 - 10\ s^{-1}$ depending on the temperature and high voltage (HV) bias, which is more than 2 orders of magnitude times less than the expected minimum counting rate due to the heliospheric glow.

GLOWS plans to perform science analysis on (1), and all the other ones need to be identified and subtracted. (3) is planned to be used for absolute calibration, so that the global long-time evolution of (1) can be distinguished from the effects of the inevitable gradual loss of the detector sensitivity during the mission.

2.3 Science Requirements

GLOWS is expected to provide latitudinal structure of the solar wind with the time resolution comparable with the travel time of typical heliospheric ENAs from the termination shock to 1 au over the entire duration of the IMAP mission. The travel times of ENAs from 100 to 1 au vary with the ENA energy from ~ 1250 days for 0.1 keV ENAs through ~ 400 days for 1 keV ENAs down to ~ 40 days for 100 keV ENAs.

Based on the retrieved profiles of the speed and density of the solar wind, survival probabilities of ENAs observed daily by IMAP-Lo, IMAP-Hi, and IMAP-Ultra must be calculated for each IMAP pointing.

To facilitate achievement of these goals, the design must minimize contributions to the signal from extraheliospheric sources and maximize that of the helioglow itself. The daily signal from the helioglow must be statistically significantly stronger than those from the other sources, and when this is not possible, then the unwanted signals must be identified and masked or portions of the data with excessive background must be culled.

GLOWS counts individual photons, so its sensitivity must be sufficiently high to guarantee that statistical scatter of the collected data is low enough ($<\sim 1\%$) to enable meaningful measurements of the helioglow. Additional contributions of Lyman-α radiation from the outside of the instrument FoV, in particular from the Sun, must be attenuated to a level comparable to the magnitude of statistical scatter of the helioglow signal. Furthermore, it must

guarantee sufficient statistics for analysis of calibration stars after subtraction of the helioglow (Sect. 5.2) for a total daily observation time of 20 hours for the adopted binning of the lightcurve (see Sect. 2.3.2).

These requirements were the main driver for the design of the instrument and measurement process, as discussed in the following subsections.

2.3.1 Observation Geometry

GLOWS collects the signal from rings in the sky centered at the IMAP spin axis (see the bottom left panel in Fig. 1). The radius and width of the scanning circle must maximize the time during the year when the effects of the latitudinal anisotropy of the solar wind are most pronounced in the lightcurves. The lines of sight should intersect the region in space where most of the imprint of the solar ionization is exerted on the ISN H gas. This implies that the lines of sight must intersect the maximum emissivity region, i.e., geometric locations for which $n_{\mathrm{H}}(r)/r^2$ (density of ISN H divided by solar distance squared) attains its maximum as a function of r, which is typically $\sim 2-4$ au (except for the downwind region, see Kubiak et al. 2021a). The distance of intersection of the solar polar axes for observations along the lines of sight anchored in the ecliptic plane and inclined to the Sun's direction at ρ is given by $\tan\rho$; the scanning circle radius ρ must be chosen so that ρ corresponds to the distance of the maximum emissivity region.

For $\rho > 90°$, the lines of sight would miss the maximum emissivity region altogether. During approximately half of the year, the observed portion of ISN H would be before the passage above the solar poles, where most of the ionization anisotropy imprint is expected to occur. Thus, ρ must be $< 90°$, i.e., the scanning circle must be located in the solar hemisphere.

The scanning circle should coincide with the Galactic plane as little as possible over the year to minimize the time when observations have strong extraheliospheric background. For the radii much smaller than 75°, the scanning circle could be far from the Galactic disk most of the time, but the Sun would be too close to the instrument boresight for effective suppression of its stray light and the requirement of intersection of the maximum emissivity region would be not fulfilled.

These considerations resulted in adoption of the GLOWS scanning circle radius at $\rho = 75°$. Example locations of the scanning circles in the sky (for vantage points upwind and crosswind) are shown in Fig. 1.

2.3.2 Field of View and Angular Resolution

The radius of the instrument FoV and the resolution of the observations as a function of spin angle are driven on one hand by the demands of data analysis and on the other hand by the need of tracking the evolution of the instrument sensitivity in flight, while maintaining the statistical scatter of the observations much smaller than the expected relative variation in the lightcurve due to ionization anisotropy. The latter quantity is expected to be on a level 15–30% (see the lower panel of Fig. 1).

The diameter of the adopted light-sensitive element of the detector (the channeltron funnel) is 2.54 cm. The need for simplicity and low mass and cost of the optical system excludes the use of light-focusing elements. Thus, the FoV must be sufficiently large to collect enough light from the helioglow to guarantee a sufficient photon statistics. On the other hand, it must be much smaller than the expected angular scale of variation of the helioglow in the sky. A relatively small FoV also facilitates simulation of the signal, without the need for integration

over large portions of the sky. After extensive studies, we found that a good compromise is a full width at half maximum (FWHM) of the FoV of $\sim 4°$.

The adopted lightcurve binning scheme should minimize correlations between neighboring bins. This requires relatively wide bins in comparison with the FoV radius. However, the bin width must be smaller than the angular dimension of the features of the lightcurves.

Another driver for the bin width is maintaining the ability to measure the absolute brightness of stars, needed to track the instrument calibration. To that end (see Sect. 5.2), it is desirable to have a very fine binning, much finer than the width of the instrument point spread function (PSF), so that it is possible to track the brightness of a star as it traverses the FoV. The lightcurve for the star would then paint the instrument PSF. We estimated that a resolution of 40 bins within the 4° FoV is sufficient for this purpose.

Hence the adopted baseline resolution of the lightcurves is 3600 bins for the scan circle, i.e., 0.1°. This high resolution is planned only for measurements of star brightness. For retrieval of the solar wind structure, data decorrelation will be performed by rebinning the lightcurves to a resolution of 4° after masking out stars and the Milky Way. This approach facilitates measurement of star brightness and rejection of the star-contaminated portions of lightcurves while maintaining maximum information on the solar wind imprint in the lightcurves.

2.3.3 Stray Light Suppression

Analysis of the lightcurves requires a good understanding of the sources of the measured signal, in particular, of the physical background. This requires suppression of stray light, i.e., photons from the outside of the FoV.

Stray light must be minimized to the level approximately equal to that of the statistical scatter. The intensity of direct Sun light for the Lyman-α bandwidth exceeds that expected from the helioglow by a factor of $\simeq 10^8$. This implies that the optical system must provide a suppression factor for the Sun located $\sim 70°$ away on the order of 10^{10}. This strong suppression must be achieved only at the Sun side. For stellar sources, which are brighter than the helioglow up to a factor of ~ 10, suppression by a factor of ~ 1000 at an angular distance from the instrument boresight twice that of the diameter of the FoV is required.

Another potential light source in the instrument aperture is light reflected from spacecraft parts. To guarantee that the Sun- or star light reflected from the spacecraft does not enter the instrument, it is required that no part of the spacecraft is within the GLOWS field of regard (FoR), defined as the half sphere with its base in the plane of the baffle hood's aperture, as illustrated in Fig. 4.

2.3.4 Spectral Bandwidth

Maximization of the helioglow signal relative to that of the extraheliospheric sources is the driver for spectral suppression requirements. The contribution from the unresolved extraheliospheric background is required to be not larger than the expected statistical scatter. The extraheliospheric background is spectrally wide in the EUV, while the helioglow is almost monochromatic. Due to the Doppler effect, the spectral width of the observed helioglow for individual lines of sight is governed by the spread of the distribution function of ISN H projected on the line of sight. It was verified (Kubiak et al. 2021a) that it is typically close to 10 km s^{-1}, which is equivalent to a Doppler bandwidth of 0.44×10^{-2} nm. The ISN H gas flows past the Sun in the maximum emissivity region at a speed of ~ 30 km s^{-1} (Bzowski et al. 1997), equivalent to a Doppler shift of 1.2×10^{-2} nm. For the adopted geometry of

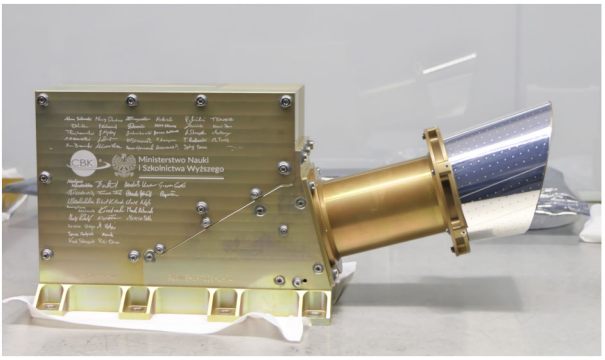

Fig. 2 GLOWS flight model, with signatures of the GLOWS team and logos of the Polish Ministry for Science and Education and CBK PAN

observations, the largest differences in the wavelength of the helioglow are expected at the crosswind positions of IMAP, when ecliptic longitude of the spacecraft differs from that of the flow direction of ISN H, equal to $\simeq 252°$ (e.g, Bzowski et al. 2023), by 90°. Then, the wavelengths of the observed helioglow for the lines of sight located in the ecliptic plane at the upwind and downwind sides will be different from each other by $\simeq 2.4 \times 10^{-2}$ nm. This wavelength span is extremely small in comparison with the spectrum of extraheliospheric astrophysical sources.

Thus, suppression of extraheliospheric background requires a narrow bandwidth of the instrument on one hand, but with a relatively flat maximum within $\simeq 2 \times 10^{-2}$ nm from the Lyman-α wavelength equal to 121.567 nm. Additionally, the wavelength selection system is desired to be simple and low-cost. This resulted in the decision of application of an interference filter (see Sect. 3.1.2).

3 Instrument Description

GLOWS is a single pixel Lyman-α photometer designed to measure the intensity of the heliospheric Lyman-α glow. The flight model of the instrument is shown in Fig. 2, and its main parameters are collected in Table 1. GLOWS is conceptually based on the TWINS/LaD photometer (Nass et al. 2006; McComas et al. 2009a), originally designed to observe the geocoronal Lyman-α glow. The main components of the instrument include the optical entrance system, detector system, electronics block, and power supply system.

The entrance system comprises a collimator, a baffle with a sunshield, and a spectral filter. It admits photons from the desired FoV and spectral band to the detector system. The detector converts photons impacting its active surface into event pulses. The electronics block collects the event pulses and stores them in data histograms. The power supply system includes a low-voltage power supply for feeding the entire instrument and a high-voltage power supply that converts the voltage to the level required by the detector system. The data histograms are forwarded to the telemetry system of the IMAP spacecraft for downlinking to the Earth.

The detector section includes a channel electron multiplier (CEM), connected to the Front-End Electronics (FEE) unit. This unit collects voltage impulses from the detector and converts them to digital events that are handed over to the Digital Processing Unit (DPU) for processing and storing. The global view of the instrument is presented in Fig. 2, its block diagram in Fig. 3, and a cross section in Fig. 4.

Table 1 GLOWS performance parameters

Parameter	Performance
Instrument type	Lyman-α single-pixel photometer
Species	Hydrogen helioglow lightcurves
Waveband	120.5 nm $\pm$ 4.25 nm HWHM
Scanning circle radius	75°
Field of view	circular, radius 4.2°
Sensitivity	3.37 cps/Rayleigh
Total mass	3.70 kg
Dimensions	380 mm (L) x 165 mm (H) x 132 mm (W)
Total power	5.1 W
Usable HV range	1500 V – 2500 V
Total downlink rate	1200 bps

Data collection-related parameters are presented in Table 3

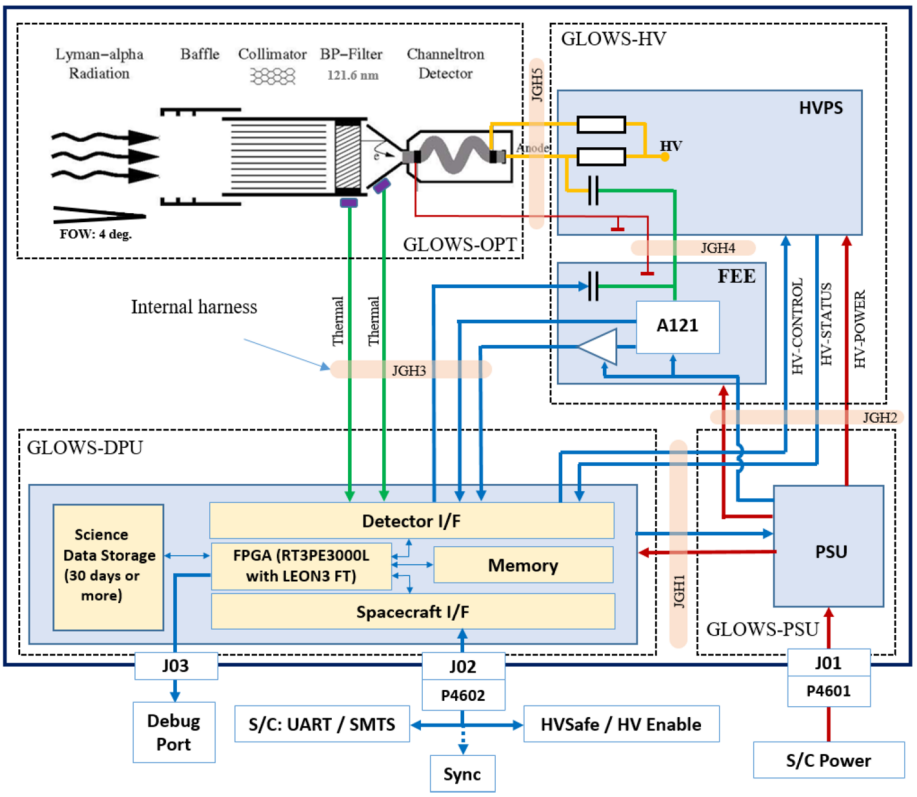

Fig. 3 Block diagram of the GLOWS Lyman-α photometer

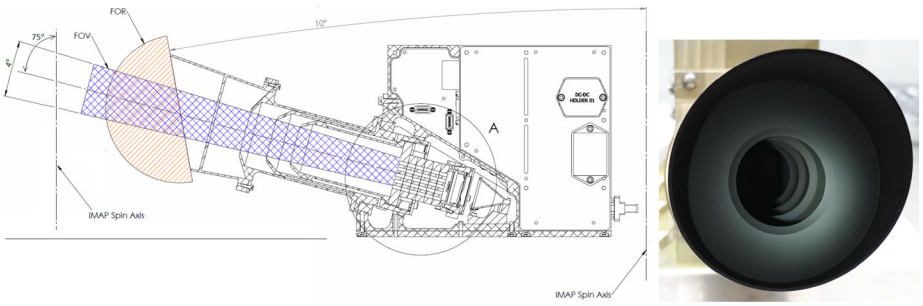

Fig. 4 Left: cross section of GLOWS. The blue-hashed volume marks the region of free access of photons to the detector. It corresponds to the effective FoV. The orange region, defined by the sunshield, marks the FoR, which must be kept free from any objects, in particular the Sun, Earth, and Moon. The collimator, optical filter, Ni mesh, and detector are located to the right from the blue-hashed region. Right: a slightly off-center photo of the entrance to the blackened flight-model baffle, with individual diaphragms visible

3.1 Optical Entrance System

The key components of the optical path include the baffle and collimator that define the FoV and the point-spread function (PSF), an optical filter that defines the spectral bandwidth of the light admitted to the detector section, and a grounded nickel mesh that helps control the electric field between the filter and CEM and prevents intrusion of photoelectrons emitted from the filter into the CEM.

3.1.1 Baffle and Collimator

The collimator plays the central role in defining the FoV. The angular width of the FoV is determined by the radius/length ratio of the optical tubes. To safeguard a sufficient area of the circular active surface of the detector (~ 5 cm^2) and the desired FoV of $\sim 4°$ and to keep the length and mass of the entrance system reasonable, the collimator was designed in the form of a mesh of parallel optical channels ("tubes"). Analysis showed that the surfaces of the optical channels must be blackened to ensure appropriate suppression of stray light.

The tubes are 3 mm in diameter and 42.7 mm long. To facilitate blackening, the collimator was designed as a cylindrical structure assembled from six slices, each with 69 tightly packed co-aligned circular apertures (see Fig. 5), which cover the active surface of the detector. The minimum thickness of the walls between the tubes is 0.1 mm.

The collimator tubes were first drilled with a diameter of ~ 2.8 mm and subsequently finished by milling to 3 mm. This technology reduced the risk of plastic deformation of the thin walls between the tubes. The precision of the manufacturing of the collimator slices was verified by measurement. It was found that the actual positions of the tubes agree with the design within 20 μm, deviations of the axes of the tubes from perfect vertical alignment are less than 0.08°, the diameters are larger by 5–12 μm than specified, the tubes do not show signatures of conical shape, departures from circularity are typically less than 6 μm and, most importantly, there are no openings between the neighboring tubes. Details of the design, manufacturing, and verification are available in Kowalski (2020).

Analysis showed that the collimator itself is not able to prevent sunlight from reaching the detector when the angle between the optical axis and the Sun's limb is less than 90°. Moreover, $\sim 4\%$ of the signal measured by the detector would be from the outside of the desired FoV even in the absence of sunlight. Thus, to prevent stray light, the instrument

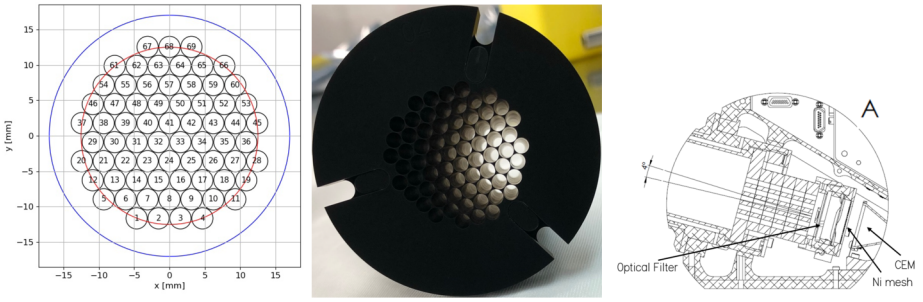

Fig. 5 Arrangement of the collimator tubes (left), a slightly off-axis view of the assembled collimator unit (center), with the blackening applied, and details of mounting of the collimator with the optical filter and the grounded mesh mounted between the filter and the CEM opening (right). The red circle in the left panel marks the perimeter of the active surface of the CEM detector. The offset view of the collimator of the center panel illustrates the uneven light transmission between the collimator tubes at an off-axis geometry

is fitted with a specially designed baffle with a sunshield (see Fig. 4; Kaźmierczak et al. (2021)). The baffle comprises a system of diaphragms (see the right panel of Fig. 4) that form traps for photons entering the baffle from directions outside of the desired FoV while admitting those from within the desired FoV. The angle of the opening of the sunshield (see the left panel of Fig. 4) prevents sunlight from entering the baffle for all operational angles between the IMAP rotation axis and the Sun's limb. The effective point-spread function of the optical entrance system is discussed in Sect. 5.1.2.

The collimator and baffle elements are made of 6061 Aluminum and contribute to the instrument's structural integrity (Barciński et al. 2024). The optical surfaces are blackened with Acktar Magic Black™ coating to reduce light reflections and constrain the effective FoV. The outer surfaces are chromate-coated for enhanced durability. The GLOWS optical system's FoR forms a half-sphere (see the orange-hatched region in the left panel of Fig. 4), and the FoV has a conical shape with a facet angle of 4° (see the blue-hatched region in the left panel of Fig. 4).

A grounded 70 LPI Ni mesh is strategically placed between the filter and the active surface of the CEM to intercept free electrons induced from the optical filters (see the right panel in Fig. 4).

3.1.2 Optical Filter

The spectral bandwidth of the instrument is defined by a convolution of the spectral transmission function of the optical interference filter and the quantum efficiency of the CEM detector. To satisfy the science requirements (see Sect. 2.3), it was potentially possible to use either a narrow interference filter or an optical grating system. A grating system would provide an extremely narrow spectral bandwidth, but also a very narrow FoV (Broadfoot 1976). The extremely narrow spectral bandwidth would result in a reduction of the visibility of calibration stars, as evidenced by observations of the helioglow by Mariner 10 (Broadfoot and Kumar 1978), so that tracking the calibration during the mission could be problematic. Furthermore, a much more complex design of the entrance system would be needed. Thus, for GLOWS, we decided to use a design with interference filter and selected the model Acton FN122-XN-1.2D, with the peak transmission $\sim 13.75\%$ at 121.5 nm and a FWHM bandpass equal to ~ 8.5 nm, as declared by the manufacturer and verified during the calibration.

3.2 Detector System

The detector system comprises a channel electron multiplier and a dedicated front-end electronics subsystem.

3.2.1 Channel Electron Multiplier CEM

Channel electron multipliers are high-performance photon and particle detectors for applications requiring precise single-event detection. They operate by amplifying electrons ejected from the active surface by the incoming photons. The ejected electron is accelerated to a sufficient energy to extract more electrons on impact on the CEM funnel walls. These new electrons are also accelerated, generate new free electrons, etc. Eventually, a cascade of secondary electron emissions is formed. The electron cascade is generated when the high voltage applied to the CEM electrodes exceeds a certain value. This cascade generates a measurable impulse at the CEM's output. The gain (multiplication factor) necessary to register a photon event is between 10^6 and 10^8.

To function effectively, CEMs require a high-voltage bias, typically in the range of 1–3 kV. This high voltage must be carefully stabilized to ensure consistent performance and avoid damage to the device. The CEM yield is a function of the voltage and of the total processed electric charge. The characteristics has a leg-like shape, starting with a negligible yield for low voltages (foot), which transition into a linear increase segment and subsequently flattens asymptotically at the knee to a maximum value (see Nass et al. (2014), Fig. 4.2). The optimum magnitude of the operational voltage is above the knee, which for the flight unit has been measured at $\sim$ 1.7 kV. GLOWS uses the CEM model KBL25RS/90 PAN V2, custom-designed by Dr. Sjuts Optotechnik GmbH. Its active surface is conical in shape, with a circular base 1 inch (25.4 mm) in diameter.

It is expected that with the increasing collective charge processed by the CEM, its gain will be slowly degrading, requiring shifting towards higher voltage values. To maintain the yield, the operational voltage will be carefully increased. To verify the yield, in-flight calibration will be periodically performed (see Sect. 5.2).

Illumination of a CEM with a high EUV photon flux when an HV bias is applied must be avoided because it rapidly increases the total charge processed by the unit and thus reduces its lifetime. Lifetime protection of the CEM is achieved by operational procedures that do not expose the CEM to direct solar or lunar illumination. As a last-resort measure, a dedicated logic inside the FPGA provides a protection that cuts off the HV bias when it detects a count number greater than 2 000 events collected during 0.1 s.

The gain characteristics of the GLOWS CEM is presented in the left panel of Fig. 7. The spectral efficiency of the detector is obtained from convolution of the quantum efficiency of the CEM with the filter transmission function (see Sect. 5.1.1).

3.2.2 Front-End Electronics System FEE

The GLOWS front-end electronics system (FEE) is a critical module designed to condition the signal generated by the CEM to voltages detectable by the FPGA chip in the DPU (Sect. 3.3). It acts as an interface between the CEM and DPU, enabling detection and processing of individual photon events.

When a photon impacts the active surface of the CEM, a small voltage impulse is generated at the electrodes. The FEE amplifies this impulse and eliminates events considered as invalid based on a user-defined voltage threshold THRS set by the DPU. This ensures

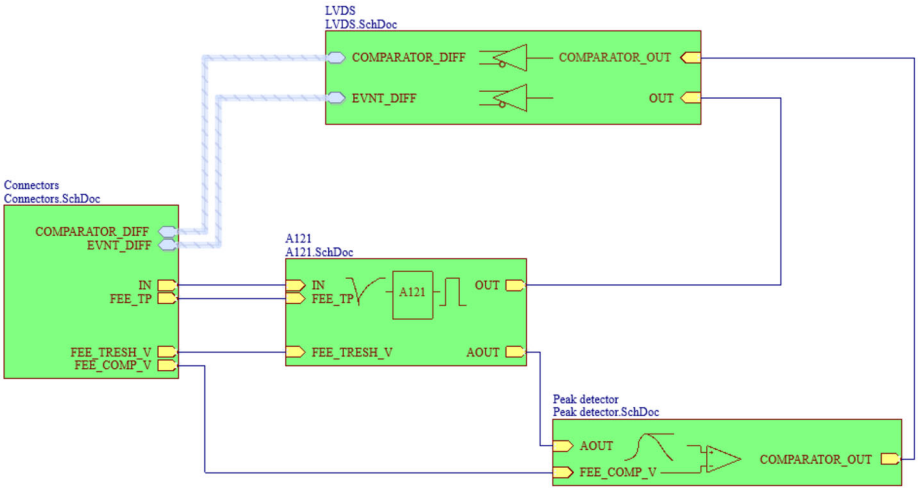

Fig. 6 Block diagram of the GLOWS FEE

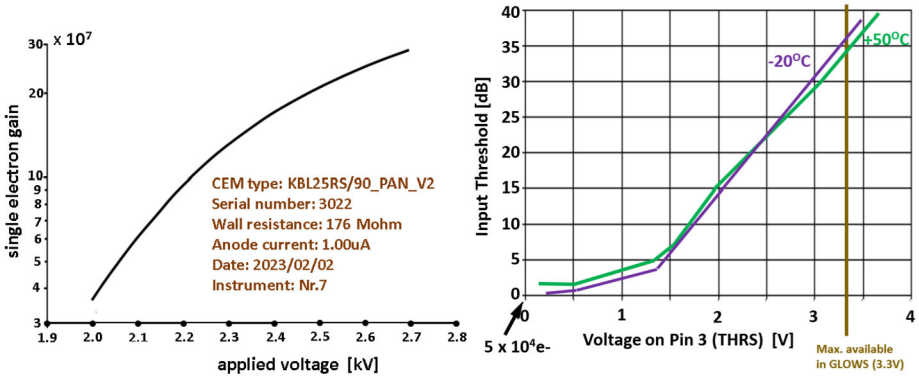

Fig. 7 Gain (multiplication factor) of the CEM used in the GLOWS FM as a function of the voltage applied (left panel) and the threshold level for charge detection vs the THRS voltage applied to pin 3 of Amptek A121 (right panel)

that only valid data are captured and transmitted. The primary component of the FEE is the Amptek A121 chip, a hybrid charge-sensitive preamplifier-discriminator optimized for fast pulse counting applications with CEMs. It provides the following two outputs:

- a digital output, where each pulse represents a photon detected by the CEM, and
- an analog output, which is proportional to the charge amplitude of the detected event.

A block diagram of the GLOWS FEE is shown in Fig. 6.

The digital output of the Amptek A121 delivers fixed-width pulses, each corresponding to an individual photon impact. These signals are further processed to reduce noise and ensure stable transmission to the DPU using Low Voltage Differential Signaling (LVDS) method. This method minimizes interference and guarantees reliable data transmission. The pulse width can be customized using an external resistor. For GLOWS, it is set to 240 ns.

The dead time, defined as the minimum interval required to distinguish two consecutive signals, is 400 ns.

The analog output provides information about the charge of each detected photon. To convert its output into a pulse width for further processing, the FEE employs a peak detector circuit with a comparator. At first, the analog signal undergoes conditioning by removal of DC offset using a coupling capacitor. Then, subsequent pulse shaping is performed by operational amplifiers. This conditioned analog signal is then converted to a pulse width by a comparator controlled by a secondary reference voltage COMP, which is controlled by the DPU. This process converts the signal from an amplitude representation to the time domain, making it suitable for detection by the FPGA at the DPU.

The GLOWS FEE also features a self-testing functionality to verify the system integrity. A test pulse, generated by the DPU and attenuated through a PI attenuator, simulates photon interactions at the input. This allows for validation of the FEE's signal conversion chain under controlled conditions without HV enabled.

3.2.3 Direct Event Detection Mechanism

The quantum efficiency of the GLOWS detection chain depends on the following two factors:

- the probability of ejection of an electron from the active surface of the CEM on photon impact and the subsequent generation of an electron cascade; and
- the probability of identification by the FEE of the photon-related impulse generated at the CEM output as a valid count.

The first factor depends directly on the magnitude of the gain, which varies with the high voltage (HV) applied to the CEM, as shown in the left panel of Fig. 7. The second factor is influenced by the threshold voltage THRS, which qualifies impulses as valid if their amplitudes exceed a predefined threshold value. The threshold value is a function of the voltage at one of the pins of the Amptek 121 chip and is weakly dependent on the temperature (see the right panel in Fig. 7). Thus, the quantum efficiency QE of GLOWS depends on the following settings of the instrument electronics:

- HV, which is the high voltage applied to the CEM detector and controls the gain of the detection chain,
- THRS, which is the threshold voltage and defines discrimination for electronic pulses associated with photon detection events.

The comparator voltage (COMP, Sect. 3.2.2) is a secondary parameter that does not affect the GLOWS detection pipeline unless the length of the registered pulse is longer than the time between two consecutive events. In such a case, it artificially extends the dead time of GLOWS when such multi-events occur. The registered pulse length, which is a function of COMP and event energy, is a source of information on the nature of a given detected event. This information is available from post-processing of downloaded direct events. A more important role of this mechanism is to trigger automatic HV ramp-down in the case of oversaturation of the CEM. It is supplementary to the safety feature based on the count rate limit (Sect. 3.2.1). An extremely high number of photons in a short time interval may result in detection of a decreasing count rate in the signal due to impulse overlapping, while in reality the event rate is alarmingly high. However, when the lengths of detected impulses exceed a programmed level, a programmed protection mechanism is triggered and the HV on the CEM is disabled.

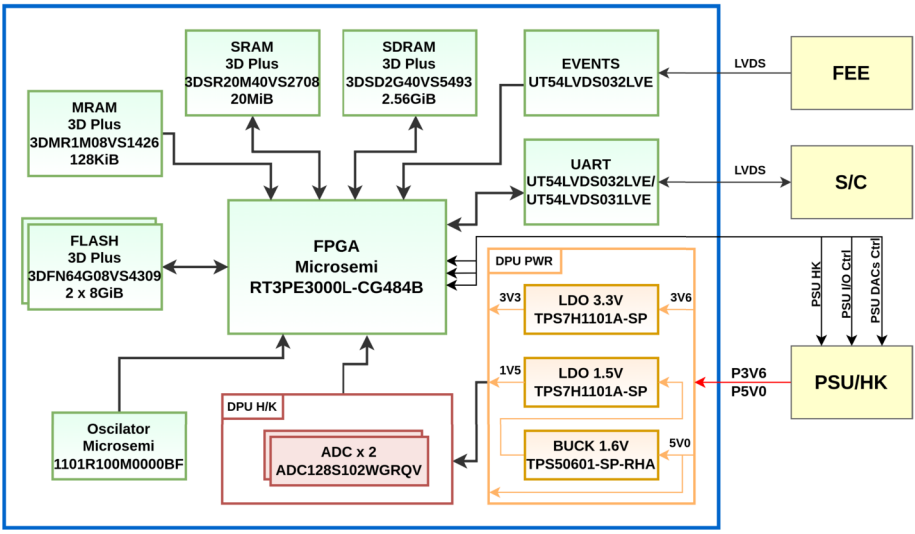

Fig. 8 Design diagram of the GLOWS Digital Processing Unit (DPU)

All of these event-detection parameters are adjustable and are planned to be set during the commissioning phase. Results of regular in-flight tests (see Sect. 6.2) may trigger a decision to modify these settings.

3.3 Digital Processing Unit

The design of the GLOWS DPU is based on heritage from the STIX experiment onboard the ESA Solar Orbiter mission (Krucker et al. 2020) and the SWI DPU for the ESA mission JUICE (Hartogh et al. 2013). A block diagram of the GLOWS DPU is shown in Fig. 8.

The GLOWS DPU provides and/or supports: an operational environment for the flight software, control interfaces for GLOWS subsystems, science data acquisition pipeline, health monitoring, and communication UART interface. The top-level functions of the DPU hardware include:

- Communication with the spacecraft over UART link;
- Control of the PSU outputs (Sect. 3.4.1);
- Control of the HVPS HV output (Sect. 3.4.2);
- Control of the FEE's detection chain signal conditioning voltages (Sect. 3.2.3);
- Detection of events on FEE interfaces (Sect. 3.2.2);
- Health monitoring of the instrument's electronics;
- Automatic isolation of faults detected in housekeeping, e.g., oversaturation of the CEM detector (Sect. 3.2.1);
- Providing storage capabilities for surplus generated data;
- Software Environment.

The FPGA chip used on the GLOWS DPU is the radiation tolerant Microsemi RT ProASic3E RT3PE3000L-CG484. The chip was selected based on its performance and power consumption. The FPGA hosts a single LEON3FT (SPARC V8 architecture) core from Gaisler AB. The processing system operates at a frequency of 20 MHz. Synthesized logic provides

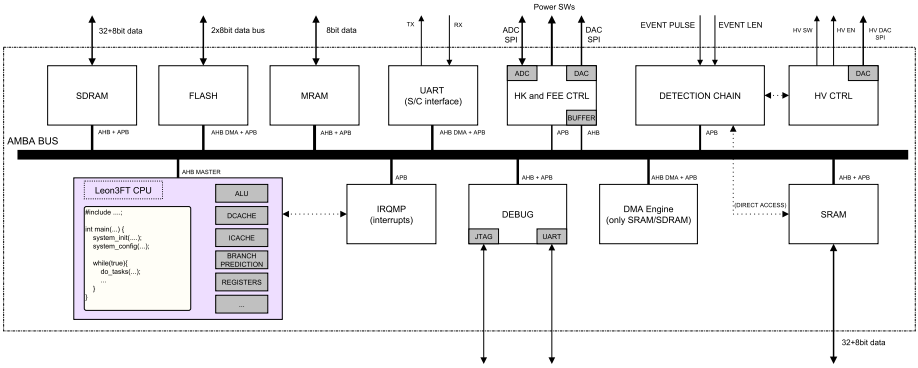

Fig. 9 Design diagram of the GLOWS DPU FPGA

dedicated controllers for all DPU memories, UART communication link, housekeeping, Test Pulse generation, FEE readout from the CEM detector and control of the HVPS HV output. The overall architecture of the GLOWS DPU FPGA is shown in Fig. 9.

GLOWS Flight Software is divided into three main packages:

- Board Support Package (BSP) – low level drivers, with direct links to the GLOWS custom hardware (used only by BootSW).
- Booting Software (BootSW, BSW) – boot strap + startup software. Resides in the non-volatile MRAM memory and is loaded by default after power on. It supports only limited scope of TC/TMs and is intended to load Application SW, but by itself it does not perform any science operations. In the Flight Model, it is not possible to reprogram the host memory, so this software item is not patchable;
- Application Software (AppSW) – supports all defined TC/TMs and performs science operations. AppSW images are stored in NAND FLASH (with CRC and redundancy) and the program itself is patchable during the mission. AppSW uses RTEMS as the Real Time Operating System for tasking, scheduling, and memory management.

The GLOWS transitions autonomously into the SCIENCE mode ~ 45 seconds after instrument power on, power cycle, or reset sequence.

3.4 Power Supply System

3.4.1 Low-Voltage Power Supply LVPS

The Power Supply Unit (PSU) was custom-designed for GLOWS (Fig. 10). It ensures a stable, reliable, and regulated power delivery to the HVPS (Sect. 3.4.2), FEE (Sect. 3.2.2), and DPU (Sect. 3.3).

The PSU provides seven voltage channels carefully tailored to meet the specific requirements of their designated modules and ensure noise-free operation. The core power outputs include 5 V, 12 V, and -12 V, generated through isolated DC/DC converters. These outputs are further regulated into secondary voltages, such as 3.3 V and -5 V, using Low Dropout Regulators (LDOs).

The HVPS and FEE modules can be remotely activated and deactivated via dedicated control mechanisms. Voltage adjustments for high voltage output, threshold settings for amplifiers and analog output controls are implemented through digital-to-analog converters

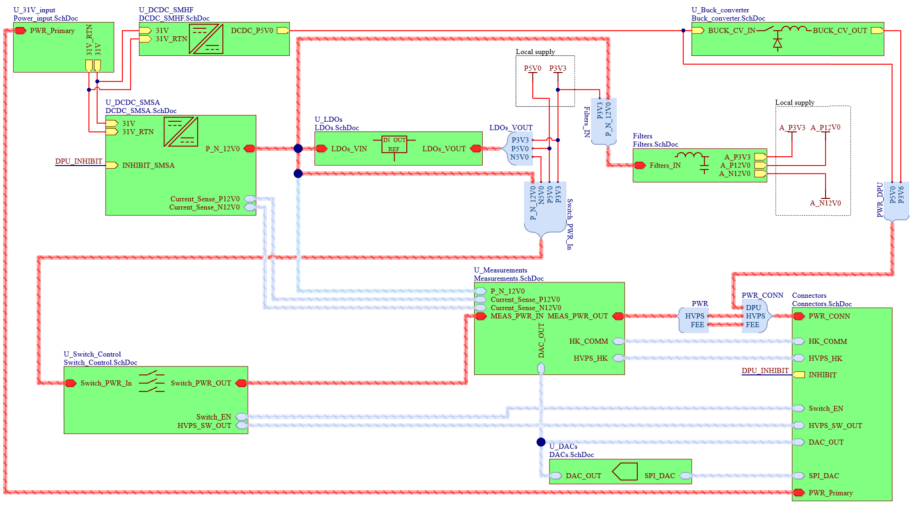

Fig. 10 Block diagram of the GLOWS power supply unit (PSU)

(DACs). The real-time diagnostics is implemented in DPU. The diagnostics logic takes data from Analog-to-Digital Converter (ADC) and continuously monitors currents, voltages, and temperatures. To increase the number of monitored channels, a multiplexer was incorporated. The temperature monitoring system employs strategically placed sensors to measure critical points, including the DC/DC converters, the PSU's printed circuit board (PCB), and the HVPS module.

To maintain the integrity of sensitive electronic components, the PSU is equipped with Electromagnetic Interference (EMI) filters that serve as a protective barrier, mitigating potential electromagnetic interference.

3.4.2 High Voltage Power Supply HVPS

The GLOWS HVPS is used to provide the CEM with the high voltage it requires to function. The HVPS houses one supply on a single board: one programmable CEM supply (see the right-hand panel in Fig. 11). The HVPS board interfaces with the LVPS and the CDH through a single 15-pin Micro-D connector. The HV produced by the HVPS is routed to the instrument via a shielded coax cable. The supply on the board is subject to an enable signal, which enables/disables the high voltage power supply, as well as a V/10 signal, which reduces the output voltages to approximately 10% of their programmed voltage. The diagram in the left panel of Fig. 11 shows the connections between the HVPS and the simulated CEM circuits.

The supply's topology is a resonant flyback converter with Cockcroft-Walton multiplier and a custom-designed pulse width modulator for high voltage low power applications. The topology was chosen to deliver a low noise output that is programmable via an analog signal from 0 to +5 V to obtain an output voltage from 0 V to the maximum value of 3.5 kV. An output voltage monitor is scaled from 0 V to 4.5 V for 0 V to full output with a 5 kΩ output impedance. A ±12 V voltage is supplied from the LVPS via a connector, drawing a total power of 0.336 W while delivering full voltage using the maximum loads specified.

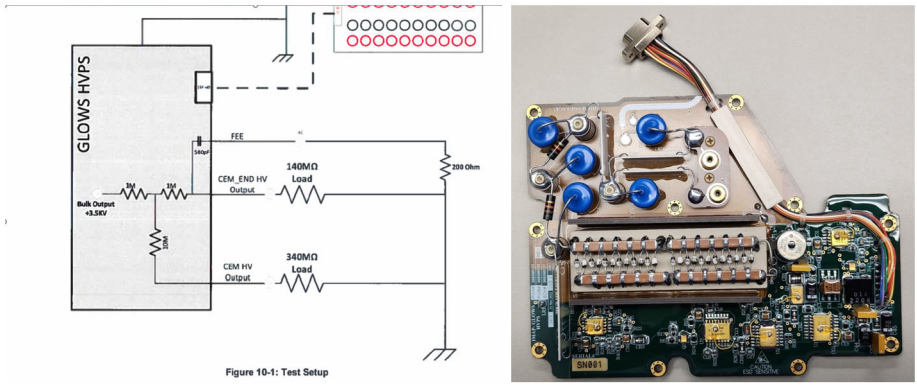

Fig. 11 Block diagram of the GLOWS high-voltage power supply unit (left) and a photograph of its electronic board (right)

4 Instrument Performance Model

Following definitions discussed by Quemerais and Bertaux (2002b) and Nass et al. (2006), we define the overall sensitivity of the GLOWS instrument in terms of the calibration factor

$$\alpha(HV, THRS, COMP, \lambda, t) = L_{1R} \times QE(HV, THRS, COMP, \lambda, t) \times A \times \Omega \quad (2)$$

that converts the count rate of the instrument in the counts per second (cps) units into the photon flux density in the Rayleigh units; $L_{1R} = 10^6/(4\pi)$ photons s^{-1} cm^{-2} sr^{-1}.

The quantum efficiency QE in cts/photon units is understood here as averaged over the GLOWS FoV for the assembled instrument. It is further discussed in Sect. 5.1.1. Settings of the instrument electronics affect QE via the voltages HV, $THRS$, $COMP$, as discussed in Sects. 3.2.3 and 5.1.3. The quantum efficiency QE depends also on the wavelength λ, which is important for determination of the instrument bandwidth and its center wavelength and for in-flight calibration tracking based on star observations, as described in Sect. 5.2. The dependence of QE on time t in Equation (2) is intended to account for the sensor aging and sensitivity degradation that are planned to be addressed by the in-flight calibration tracking, discussed in Sect. 5.2, and adjustment of the HV setting based on results of the in-flight tests discussed in Sect. 6.2.

The area A of the CEM detector is $A = 5.07$ cm^2. The effective solid angle Ω determines the GLOWS FoV and can be computed from the spherical cap formula $\Omega = 2\pi(1 - \cos\rho_{\mathrm{FoV}})$, where the angular radius ρ_{FoV} of the FoV can be found from measurements of the PSF of the instrument as discussed in Sect. 5.1.2.

5 Calibration

Successful accomplishment of the GLOWS science requirements does not require a precise knowledge of its absolute sensitivity (Porowski and Bzowski 2024). However, the sensitivity of the instrument must be tracked from the beginning of science operations, i.e., its changes during the flight must be identified and either compensated or at least registered.

Thus, GLOWS requires a two-step calibration:

- by laboratory measurements of its initial sensitivity for performance validation (ground calibration, see Sect. 5.1), and
- by in-flight tracking of sensitivity degradation based on observations of bright stars (Sect. 5.2).

General approach to the GLOWS calibration is similar to that applied to the heritage instrument TWINS/LAD (Nass et al. 2006). The flight model of the instrument was assembled using the CEM and filter selected based on the performance of individual items from several production batches, measured at PTB, WAT, and CBK PAN. Based on the results, flight items were selected. Flight spares were chosen as those with the characteristics the nearest to those of the flight items. Measurements of the angularly-dependent reflectance of Acktar Magic Black™ coating were performed at WAT using a specially developed and well-characterized double stream gas puff target VUV source on a specially developed test bench (Wardzińska et al., in prep). The results, presented by Strumik et al. (2024b), were used in numerical simulations of the optics performance, needed for final determination of the PSF in conjunction with measurements performed at PTB and CBK PAN.

The final calibration was performed on the flight model. During pre-shipment tests, the selected flight CEM malfunctioned and was replaced with a flight spare with the characteristics the closest to the original flight item. Comparison of the characteristics measured before and after the replacement showed that the sensitivity of the flight model remained unchanged.

5.1 Ground Calibration

The calibration and performance validation of the GLOWS flight model was carried out at the Metrology Light Source (MLS) of the Physikalisch-Technische Bundesanstalt (PTB) in Berlin-Adlershof, Germany. Radiometric calibration using monochromatized synchrotron radiation with absolutely determined photon flux and defined spectral characteristics was successfully applied in the past to the TWINS/LAD instrument (GLOWS heritage) and other space instruments (e.g., SOHO/SUMER, TIMED/SEE, Solar-B/EIS, Solar Orbiter/EUI, and SolarOrbiter/SPICE), formerly also at PTB's laboratories at the Berlin electron storage rings BESSY I and BESSY II. The availability of radiation over the full FUV/EUV spectral range with intensities scalable by the stored electron current and traceable to radiometric standards in combination with PTB's infrastructure is a unique premise for the reliable pre-flight calibration capability.

Some additional measurements of the PSF have been performed in CBK PAN facilities using a deuterium lamp.

5.1.1 Quantum Efficiency and Spectral Response

The monochromatized synchrotron radiation beam is comparably narrow (2×1 mm^2) and strongly collimated. Thus, performing a raster scan over the GLOWS entrance aperture was needed to characterize the aperture-averaged response of the instrument, as shown in the left panel of Fig. 12. The estimated aperture-averaged quantum efficiency of GLOWS is $\sim 2 \times 10^{-3}$ cts/photon at the Lyman-α wavelength, as shown in Fig. 12. It represents not only the quantum efficiency of the CEM itself, but also the effects of the filter, collimator, and grounding grid on the optical throughput.

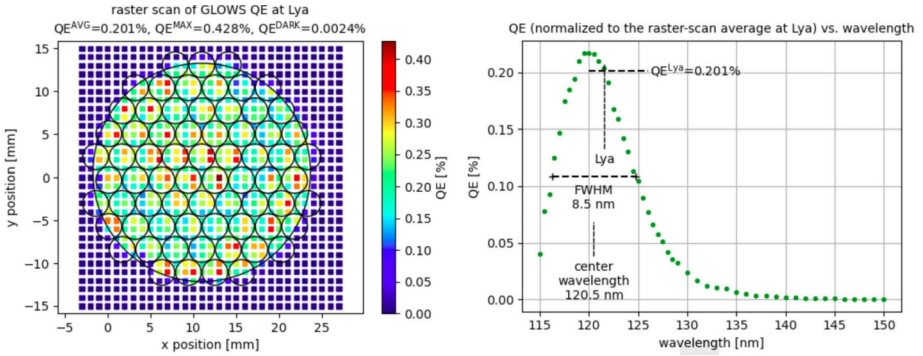

Fig. 12 Left panel: a 31 × 31-points raster scan over the instrument aperture showing measurements of the number of counts per 100 incoming photons for the Lyman-α wavelength. Right panel: spectral response of the instrument

The right panel of Fig. 12 shows results of a wavelength scan performed to characterize the spectral response of the instrument. The scan was obtained for the UV beam passing through one of the tubes of the collimator. The results were subsequently normalized to the averaged raster scan at the Lyman-α wavelength. The wavelength scan allowed us to determine the FWHM bandwidth of ∼8.5 nm and the center wavelength of ∼120.5 nm for the instrument.

The results of the raster and wavelength scans presented in Fig. 12 have been corrected for the imperfect alignment discussed in Sect. 5.1.2. Both the raster and wavelength scans have been obtained at a very low electron current in the storage ring without any attenuating filters for the UV beam. The beam intensity variation was $< 0.5\%$ on time scales of ~ 100 s, as needed for one measurement point (counts integration) during the calibration.

5.1.2 PSF – Measurements and Simulations

Similarly to measurements of the quantum efficiency, measurements of the PSF in PTB required scanning over the instrument aperture, which introduced additional systematic errors. The errors were investigated and successfully reproduced by ray-tracing numerical simulations, shown in Fig. 13 (left panel). Results of the measurement compared with simulations indicated an offset of ∼0.5° in the alignment of the UV beam with respect to the GLOWS optical axis during the calibration. This offset implies an imperfect-alignment correction of 1.27 to the raw quantum efficiency estimates, as mentioned in Sect. 5.1.1.

Independent measurements of the PSF were performed in CBK PAN using a deuterium lamp. A divergent beam from the lamp introduced systematic errors of a different kind, which have also been successfully reproduced by ray-tracing simulations, as presented in Fig. 13 (right panel).

Based on the measurements at PTB and CBK PAN and numerical simulations we inferred the PSF function of the instrument corrected for measurement errors (see "INFERRED PSF" in Fig. 13). The PSF varies approximately linearly within 3° off the GLOWS optical axis (note the logarithmic scale in the vertical axis in Fig. 13). The effective angular radius of the instrument FoV is $\rho_{\mathrm{FoV}} = 2.09°$, which gives the solid angle $\Omega = 4.16 \times 10^{-3}$ sr.

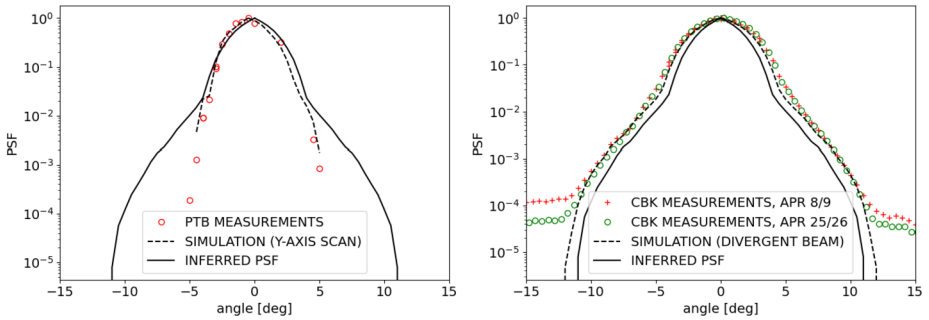

Fig. 13 Results of the PSF measurements in PTB (left panel) and in CBK PAN (right panel) compared with dedicated numerical simulations and the final inferred PSF. The horizontal axis represents offsets of the beam direction from the center. The PSF is dimensionless, with normalization to 1 at the peak

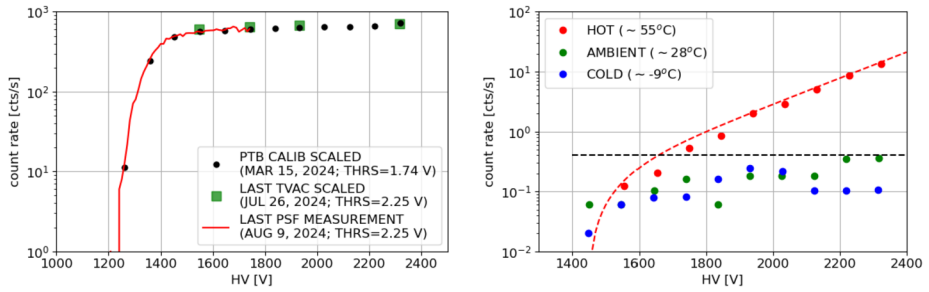

Fig. 14 Left panel: comparison of the HV gain characteristics from the PTB calibration with the last TVAC and PSF measurements at CBK PAN before shipment of the instrument. Right panel: dark counts of the instrument as a function of high voltage HV and temperature. The black dashed line represents the upper envelope for dark count rate for temperatures below 30 °C

5.1.3 FEE Settings Dependencies and Dark Counts

As discussed in Sects. 3.2.3 and 4, the sensitivity of the instrument depends on settings of the instrument electronics. The HV gain characteristics of the GLOWS instrument are illustrated in the left panel of Fig. 14. Dependencies of the instrument count rate on the parameters $THRS$ and $COMP$ have been characterized in laboratory measurements and will be included in the IMAP CMAD (McComas et al. 2025, this journal). All the dependencies of the sensitivity on HV, $THRS$, and $COMP$ display plateaus on which the instrument is planned to operate. The expected CEM degradation in flight may change the optimum settings for the $THRS$ and $COMP$ settings for the adjusted HV. Therefore, GLOWS in-flight tests are planned to verify if instrument aging effects do not necessitate an adjustment of these parameters.

Dark counts of the instrument have been characterized as shown in the right panel of Fig. 14. For temperatures < 30 °C, the dark count rate is $< 1\,\mathrm{s}^{-1}$ and displays a flat dependence on HV. For higher temperatures, the dark count rate increases with HV, thus for $HV > 2000$ V and temperatures > 30 °C background corrections might be needed, if the instrument signal-to-noise ratio decreases during the mission below expected values.

5.1.4 Instrument Sensitivity and Signal-to-Noise Ratio

Combining the results presented in Sects. 5.1.1—5.1.3 we estimate the calibration factor defined in Equation (2) as $\alpha_0 \approx 3.37 \pm 0.19$ cps/Rayleigh. The sensitivity should be understood as obtained for the Lyman-α wavelength and settings of the electronics $HV_0 = 1550$ V, $THRS_0 = 1.74V$, and $COMP_0 = 3.2$ V. Since the final operational in-flight settings can be different, the calibration factor may also slightly change as implied by the characteristics obtained in laboratory measurements.

The signal-to-noise (SNR) ratio can be computed using the minimum expected helioglow intensity of 200 R, the calibration factor discussed above, and the dark counts measurements presented in Sect. 5.1.3. For temperatures < 30 °C we obtain SNR > 1000. For higher operational temperatures (~ 55 °C), SNR decreases with HV, from SNR > 1000 for $HV \approx 1600$ V to SNR ~ 100 for $HV \approx 2300$ V.

5.2 In-Flight Calibration Tracking

GLOWS, like any EUV detector, is expected to gradually lose its sensitivity over time. To maintain high data quality, the detector sensitivity will be monitored during the flight. This will be achieved based on cyclic observations of a carefully selected group of EUV-bright stars (see Table 2) that are known to be invariable (Snow et al. 2005). Each star is visible twice during a year during intervals of several days.

The path of a star across the FoV varies from one day to another due to daily repointing of the IMAP rotation axis. Thus, the lightcurve for this star is changing daily. The observed brightness as a function of angular distance from the center of the field of view reflects the instrument's PSF, as shown in Fig. 15. The stars are identified in the observed lightcurves based on their coordinates obtained from the SIMBAD catalog (Wenger et al. 2000). The signal of the stars is extracted by subtraction of the estimated signal of the helioglow from the observed lightcurve. We use the fact that since the helioglow is smoothly changing along the scanning circle, the helioglow intensity in the bins affected by the star can be filled by interpolation using the surrounding points of the lightcurve.

By extrapolation of the measured calibration star intensities obtained for a series of angular distances of the star from the boresight direction to 0 distance, we obtain the brightness of the calibration star as it would be seen by GLOWS if it were in the center of its field of view. If the detector sensitivity remains unchanged, this brightness should remain constant during subsequent observations of the same object. In reality, the observed brightness of a given calibration star is expected to decrease over time due to the sensitivity loss. Monitoring the brightness of a set of calibration stars allows us to determine the calibration coefficients to be used to correct the observed helioglow lightcurves for the instrument sensitivity loss.

Additionally, several stars, highlighted in bold in Table 2, have IUE measurements converted to the white dwarf scale using the FLXCOR procedure from Bohlin (1996). We plan to use these stars to obtain absolute calibration of our data to express them in physical units. However, this is not necessary to achieve the scientific goals of the experiment, which are based on studying brightness variations along the scanning circle rather than its absolute brightness.

Table 2 Calibration stars

Star name	HD nr	Longitude [deg]	Latitude [deg]	Count rate
ϵ Per	HD24760	65.683	19.116	597.09
β CMa	HD44743	97.196	−41.254	1773.40
α CMa	HD48915	104.089	−39.605	53.82
ζ Pup	HD66811	138.559	−58.345	2090.52
κ Vel	HD81188	178.895	−63.717	602.18
α Leo	**HD87901**	**149.829**	**0.464**	**144.53**
δ Cen	HD105435	207.480	−44.506	523.35
α Cru	HD108248	221.865	−52.875	7313.83
α Vir	HD116658	203.840	−2.054	4305.56
η UMa	**HD120315**	**176.935**	**54.383**	**570.42**
ζ Cen	HD121263	224.947	−32.941	1027.78
β Cen	HD122451	233.787	−44.135	5618.12
δ Sco	HD143275	242.567	−1.986	644.24
τ Sco	HD149438	251.452	−6.120	1100.01
ζ Oph	**HD149757**	**249.224**	**11.391**	**123.23**
σ Sgr	HD175191	282.379	−3.450	834.62
α Pav	HD193924	293.810	−36.268	880.75
α Gru	HD209952	315.901	−32.915	223.63
ζ Cas	**HD3360**	**35.069**	**44.723**	**211.07**
η Aur	**HD32630**	**79.452**	**18.284**	**178.81**

Note: Based on Table 7.3 in Snow et al. (2013)

Note: we have omitted α Lyr because it has a very low flux in the Lyman-α band.

6 Instrument Operations

6.1 Regular Science Operations

GLOWS scans a circle in the sky centered at the spacecraft spin axis and collects events due to Lyman-α photon impacts on the active surface of the CEM (Direct Events, DE). Registration of DEs is performed over a certain number of spacecraft spins, referred to as spin blocks.

Once collection of DEs for the current spin block is completed, the DEs are histogrammed by spin phase and saved in the histogram for this block. This is performed in parallel with data collection for the next block.

In the histogramming process, the DEs are converted from the time domain to the spin phase angle domain and stored in spin angle bins of the histogram. Conversion to the spin angle domain is done assuming that the rotation of the IMAP spacecraft during the block was uniform, with the period equal to the mean value of the periods calculated based on spin phase information broadcast every second to the instrument by the spacecraft. The DEs are stored in the GLOWS file system, and completed histograms are immediately put into telemetry for downlinking.

The number of bins in the histogram is in-flight configurable (see Table 3) and the default value is $n_{\mathrm{bin}} = 3600$, i.e., the bin width is equal to 0.1°. For the default values $n_{\mathrm{block}} = 8$ and

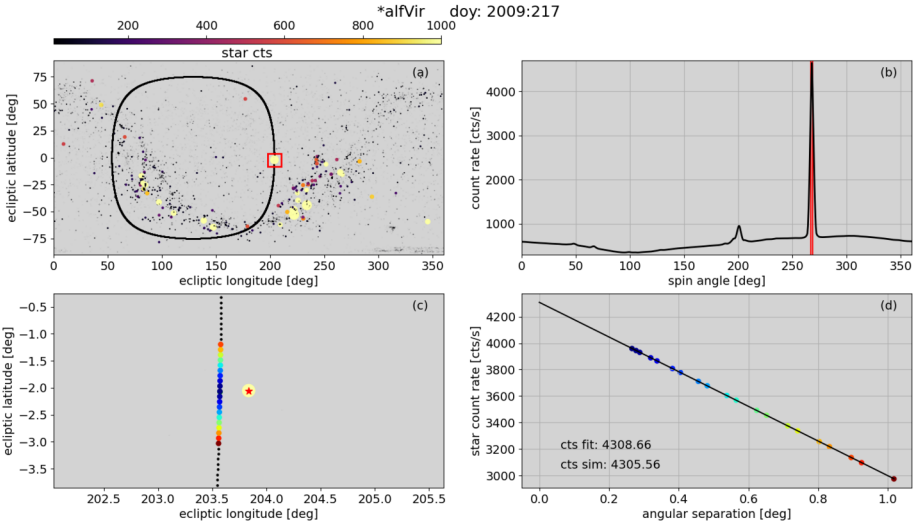

Fig. 15 Panel (a): sky map of the stars visible in the EUV band. The GLOWS scanning circle is drawn as the black circle. The red rectangle is centered at the position of the selected calibration star (in this case α Vir). Panel (b): The expected GLOWS lightcurve. The red vertical lines mark the bins affected by the calibration star signal (the same bins that are colored in panel (c)). Panel (c): zoom into the neighborhood of the selected calibration star. The colors of the bins on the scanning circle show the angular distance between the star and the center of the bin. Panel (d): Simulated count rate as a function of angular distance between the calibration star and the nearest bin on the scanning circle. The black line shows a linear fit to the simulated data

IMAP spin period $\sim$ 15 s, the time resolution of the data is 2 minutes. This facilitates removal of possible bad times in the observations during ground processing without excessive data loss.

Operations of GLOWS are governed by on-board Application Software (AppSW), which is a part of the GLOWS Flight Software (FSW) suit. AppSW implements a machine of states operating in the time domain. By default, after powering on, the FSW boots, mounts the file system, switches on the science mode, and ramps up the voltage HV on the CEM to a predetermined level and data collection begins.

By default, Science Mode is active during the entire time of IMAP science operations, but the instrument changes its state depending on the state of the IMAP Repointing Flag. The baseline state is the Day state. The instrument and spacecraft are in stable conditions, high voltage is applied to the CEM, and photon events are collected. The instrument state is changed shortly before the end of a given IMAP pointing. The sequence of states is displayed in Fig. 16.

Setting the Repointing Flag by the spacecraft indicates that thruster firings will perform the repointing maneuver in 60 minutes and triggers the Evening state in GLOWS. The instrument still collects data but starts counting down 20 spin blocks (configurable) and subsequently activates the Sunset state. The flag `is-night` is set in the histograms and the HV bias on the CEM may be decreased, if found to be necessary. The Sunset state is active during HV ramp-down. However, data are still being collected, and if the voltage is actually not changed, they are suitable for science analysis.

Subsequently, the instrument enters into the Night state. The AppSW closes the current observation day, calculates the numbers of counts for the histograms collected during the past day, identifies the blocks with the highest and lowest total count numbers, and based on

Table 3 Selected quantities related to GLOWS operations and data collection

Quantity	Denotation	Magnitude
IMAP day length (time btwn spin axis shift)	$T_{\mathrm{IMAP\ day}}$	$0.5 \leq 1.0\,\mathrm{day} \leq 3.0\,\mathrm{day}$
IMAP spin period for a given day	P_{IMAP}	15 s, inside (14.63, 15.38) s
number of IMAP spins per block[a]	n_{block}	8 (powers of 2 btwn 1 and 64)
number of bins per histogram[a]	n_{bin}	3600 (between 225 and 3600)
number of bins per histogram, science[b]	$n_{\mathrm{bin}}^{\mathrm{lores}}$	90
bin width (hi-res)[a]	b	0.1° (between 0.1° and 1.6°)
typical GLOWS counting rate[c]	s_{mean}	2000 cps
maximum expected counting rate[c]	s_{max}	5000 cps
typical counts per block[c]	C_{block}	$240\,000 \pm 490$
extreme numbers of blocks per day[d]	$\lfloor N_{\mathrm{block}} \rfloor, \lceil N_{\mathrm{block}} \rceil$	(351, 2215)
typical number of blocks per day[e]	N_{block}	720, between 702 and 738
nominal time per bin[f]	t_{bin}	4167 μs
number of bits per histogram bin	d	8 bits
average data rate for histograms (no overhead)[c]	D	240 bps (bits per second)
expected number of DEs/IMAP day[c]	C_{day}	1.7×10^8
GLOWS counter frequency	f_{counter}	2×10^6 Hz $= 2$ MHz
number of DE blocks per day put to telemetry[c]	T_{dirEv}	13
boresight azimuth off X-axis in s/c frame	ψ_{GLOWS}	217°

[a]configurable in flight

[b]configurable on the ground

[c]for the ground calibration 3.37 cps/R and absolute helioglow intensity based on SWAN calibration

[d]due to possible extremely short or extremely long IMAP days, for $n_{\mathrm{bin}} = 8$

[e]given the margin for the spin period for a nominal duration of IMAP spin axis pointing (IMAP day)

[f]for $n_{\mathrm{block}} = 8$ and $n_{\mathrm{bin}} = 3600$

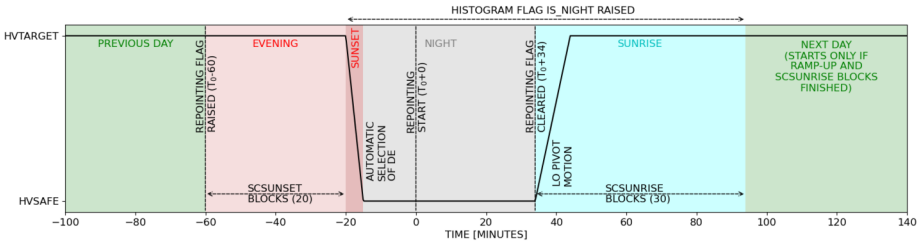

Fig. 16 Schematic representation of the transition between subsequent observation days, with a timeline demonstrating the sequence and durations of GLOWS operation modes. Note that by default, HVTARGET = HVSAFE, and thus the sunset time is equal to 0

this information prepares a list of DE data to be added to the list of DEs to be put into the telemetry system during the following observation day. The data are still collected, but they are not used in the science analysis because the observation geometry is not stable due to the spin axis repointing and subsequent nutation damping.

Resetting the Repointing flag about 34 minutes after the beginning of the spin axis repointing maneuver clears the flag `is-night` and triggers the Sunrise state in GLOWS. If the voltage was reduced, it is now returned to the former operating level. The instrument continues gathering the data but remains in the Sunrise state for another 30 blocks (configurable), waiting until the expected pivot activity of IMAP-Lo is finished. Subsequently, the Day state is triggered and the instrument remains in this state until the next Evening.

6.2 Regular in-Flight Tests

In-flight tests are performed to characterize any degradation of the instrument sensitivity over time and identify optimum settings for the current instrument conditions. They are triggered by a series of time-tagged commands at an approximately monthly cadence. Data collected during the tests are excluded from regular science analysis because the instrument is not in stable state. They are used by the science team in conjunction with results of in-flight calibration (see Sect. 5.2) to decide if a modification of the event detection parameters discussed in Sect. 3.2.3 is needed. Modification of these parameters is executed by ground commands.

The tests involve scans over the HV (1200–2400 V), THRS (1.94–3.16 V), and COMP (0.54–3.28 V) parameters. Parameter scanning is performed for one parameter at a time while keeping the other two at their current nominal values. After the scanning, the parameter is restored to its original value. The duration of the tests is about 2 hours.

The parameters are changed ("ramped") at a relatively slow rate, especially in the case of HV. Consequently, the transition time is not negligible in comparison with the actual IMAP spin period. Because parameter modifications are executed by time-tagged commands, it is not possible to synchronize the transition times precisely with the actual IMAP rotation period. Therefore, the data collection interval for each setting is set to be at least $2\times$ the nominal IMAP rotation period plus a margin of 5 s, i.e., 35 s. This guarantees that data from at least one full IMAP spin are obtained for each setting. This is done to facilitate comparison of the count numbers accumulated for full spins for each setting. It is expected that for a given parameter set, the number of counts collected during a spin is constant within the statistical scatter. Differences between the counts accumulated during full spins larger than the statistical scatter are interpreted as a result of changed parameter settings.

Data collected during these tests are marked with the `test-in-progress` flag in the GLOWS telemetry and excluded from daily-merged histograms in Level-2 data products, described in Sect. 7.

7 Data Products

Data from GLOWS include science, housekeeping, diagnostic, and supporting data products. Here, we briefly present the first category. The objective of the science data processing pipeline is to derive products well suited for further science analysis. Data processing at Levels 0 to 2 and at Level 3, along with their dependencies on external data sources, are presented in Figs. 17 and 18, respectively.

Data at Level 0 include CCSDS packets downlinked from the spacecraft. Data at Level 1A include histograms of raw counts at a time resolution $\sim$2 minutes (8 IMAP spin periods) and spin angle resolution 0.1°, and those at Level 1B are these latter histograms with ancillary data (e.g., ephemeris, spin axis direction) added.

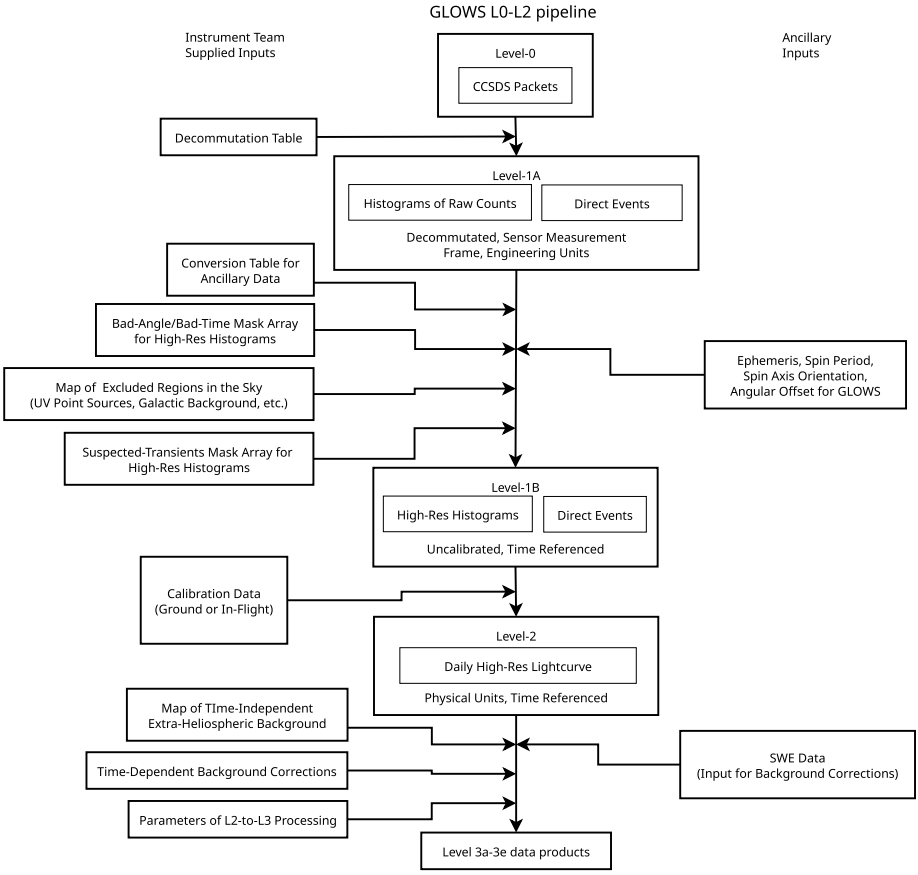

Fig. 17 A scheme of the pipeline for processing of GLOWS data from Level 0 (telemetry packets) to Level 2 (daily-averaged calibrated lightcurve)

Data at Level 2 include daily-accumulated calibrated high-resolution lightcurves (photon flux) expressed in Rayleighs as a function of spin angle, with initial culling applied, and additionally statistical uncertainties for the lightcurve elements (bins), ecliptic longitudes and latitudes of the directions in the sky for the lightcurve bins, as well as total counts and exposure times for individual bins. This product is suitable for scientific analysis, but extraheliospheric light sources are not masked and backgrounds are not subtracted.

Level 3 data are primarily intended for analysis of the helioglow and retrieval of latitudinal profiles of the solar wind speed and density, building up the history of their variations, and derived survival probabilities of ENAs observed by IMAP cameras.

Level 3A consists of a daily low-resolution (4°) calibrated photon flux with masking applied, along with total count numbers in the bins, exposure times, spin angles for the bin centers, and their celestial coordinates. Also provided are statistical uncertainties and estimates for the sky background and time-dependent local foreground in the low-resolution bins.

Level 3B consists of Carrington period-averaged heliolatitudinal profiles of the solar parameters related to ionization of hydrogen atoms at 1 au: the total ionization rate, the rates

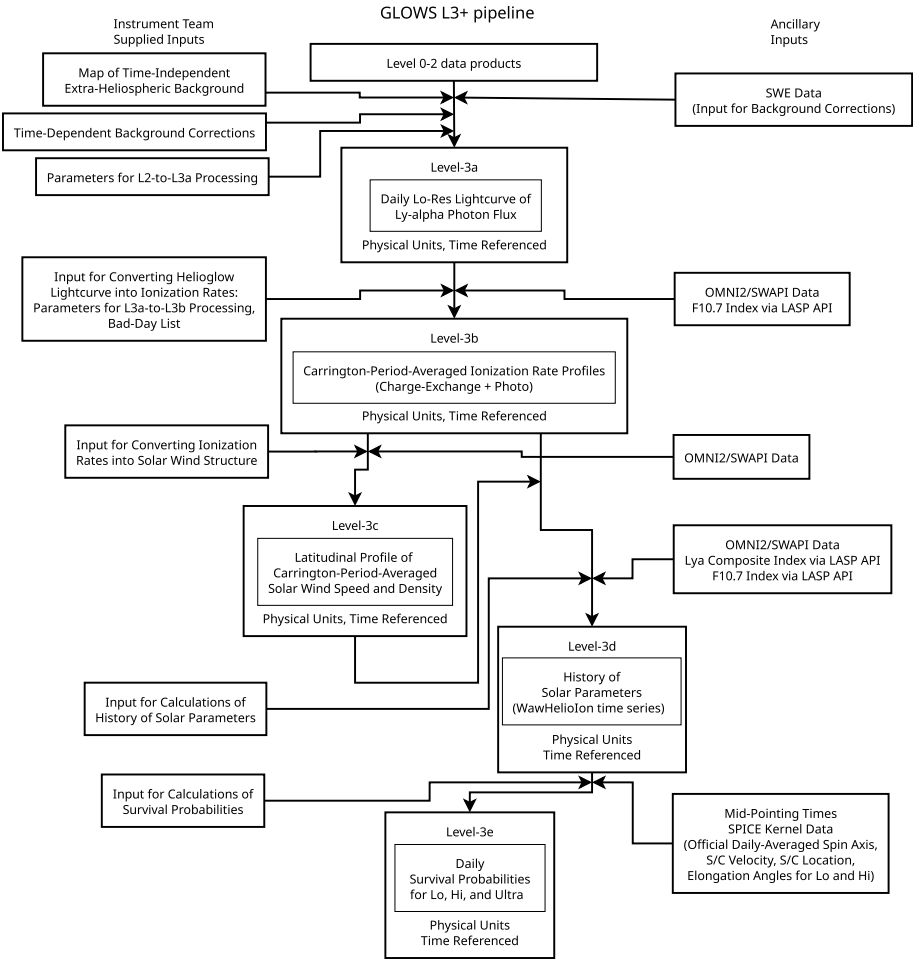

Fig. 18 A scheme of the processing of GLOWS data products within data level L3

of photoionization and charge-exchange in the stationary atom approximation, normalized profiles of the anisotropy of solar EUV emission, and the photoionization rates of H obtained as a product of the EUV anisotropy profiles and the rate of photoionization at 1 au calculated from a model by Sokół et al. (2020) using the observed solar F10.7 flux (Tapping 2013).

The ionization rate profiles are obtained based on a machine-learning approach by Porowski and Bzowski (2024) applied to daily lightcurves from Level 3A. This method relies on a relation between the profiles of the total ionization rates known from interplanetary scintillations and photoionization on one hand and the lightcurves observed by SWAN on the other hand. Porowski and Bzowski (2024) developed a mathematical method connecting these profiles, so that knowing the ionization rate profiles and the location of the observer around the Sun it is possible to predict a GLOWS-like lightcurve and vice versa, having a lightcurve observed on a specific day of the year it is possible to obtain the corresponding profile of the ionization rate based on algebraic calculations. The system was trained on

SWAN and IPS data from 3 past solar cycles. An assumption made is that statistically, the searchlights and latitudinal anisotropy of the solar Lyman-α output are related to the solar activity level. This machine-learning method is planned to be used for a fast retrieval of the solar wind structure during the mission. An in-depth analysis of lightcurves will be a separate project.

The daily profiles of the ionization rate are subsequently filtered against bad days and averaged over Carrington rotation period. Their latitudinal resolution is 10°.

Level 3C consists of products of decomposition of the Level 3B profiles of ionization rate into latitudinal profiles of the photoionization rate, solar wind speed, and solar wind density at 1 au. The speed is in km s^{-1}, and the density in cm^{-3}. The photoionization rate is assumed to be independent of heliolatitude and is calculated based on Carrington averages of the solar F10.7 flux (Tapping 2013) using a formula developed by Sokół and Bzowski (2014) and Sokół et al. (2020). Decomposition of the charge exchange ionization rate profiles into solar wind speed and density profiles is not a trivial task (see, e.g., Koutroumpa et al. 2019). In our system, it is based on an assumed latitudinal invariance of the flux of mechanical energy of the solar wind (Le Chat et al. 2012), using the cross section of charge exchange between H atoms and protons as a function of collision energy by Swaczyna et al. (2025). With the assumed latitudinal invariance, the density can be expressed by solar wind speed and the magnitude of the solar wind energy flux measured in situ in the ecliptic plane. For this, data from the IMAP/SWAPi instrument (Rankin et al. 2025, this journal) supplemeneted by those from the OMNI2 collection (King and Papitashvili 2005) will be used. Then, the formula for charge exchange becomes a sole function of solar wind speed, which can be inverted numerically.

Data Level 3D consists of the WawHelioIon model of the time evolution of the latitudinal profiles of the solar parameters needed for calculation of survival probabilities of heliospheric ENAs and simulations of interstellar neutral gas species and the helioglow: the density and speed of the solar wind, and the photoionization rates. The model is constructed so that the initial files for the speed and density, constructed based on IPS observations and solar proxies (Porowski et al. 2023), are supplemented with the profiles obtained from GLOWS observations at Level 3C. The time resolution is 1 CR, the latitudinal resolution 10°.

Level 3E consists of profiles of survival probabilities, calculated for each spin axis pointing for the actual observation geometry of IMAP-Hi90 and Hi45 (Funsten et al. 2025, this journal), IMAP-Lo (actual pivot platform pointing for the observation day; Schwadron et al. 2025, this journal), and IMAP-Ultra (Gkioulidou et al. 2025, this journal). For IMAP-Lo and IMAP-Hi, the probabilities are calculated along their respective scanning circles at a resolution of 1° on a logarithmic grid of energies starting from 0.01 keV to 19.6 keV (tuned for actual energy responses of the instruments). The data products are matrices of the probabilities for a series of energies for each spin angle. For Ultra, a sky map on a HealPix directional grid is provided, with an exclusion region of 30° around the IMAP spin axis, on a logarithmic energy grid from ~ 2.4 to ~ 356 keV being an extension of the energy grid adopted for IMAP-Hi, with an appropriate overlap. The probability product is calculated using the WawHelioIon model product at Level 3D. The probabilities are obtained by direct numerical integration of the ionization losses along trajectories of test ENAs, with the instantaneous losses (ionization) rates calculated by bilinear interpolation of the WawHelioIon products in heliolatitude and time. The system of calculation of survival probabilities is an extension of that successfully used for IBEX (Bzowski 2008).

8 Summary and Conclusion

GLOWS is a Lyman-α photometer developed in Space Research Centre of the Polish Academy of Sciences (CBK PAN) for the IMAP NASA mission. It is optimized for investigating the evolution of latitudinal structure of the solar wind based on observations of the heliospheric backscatter glow of ISN H and satisfies or exceeds all its mission requirements. GLOWS is a part of the integrated heliospheric observatory of IMAP and operates in synergy with other IMAP instruments.

GLOWS data products include daily helioglow lightcurves, as well as monthly profiles of the solar wind speed and density, and a history of the evolution of solar parameters indispensable in studies of heliospheric neutral and PUI populations and ISN gas, combined in the WawHelioIon suite. These data products are used, among others, for assessment of the attenuation of energetic neutral atoms observed by IMAP ENA instruments, as well as in the modeling of the helioglow for the past observations from other space experiments, analysis of measurements of interstellar neutral gas and its derivative population of pickup ions. The evolution of the solar wind structure obtained from GLOWS provides a context for studies of the evolution of the global heliosphere during the solar activity cycle, investigated by combination of the IMAP in-situ and remote-sensing observations, and for analysis of ISN gas observed by IBEX and IMAP, in particular ISN hydrogen.

Acknowledgements The GLOWS Science Team gratefully acknowledges insights into the realm of helioglow observations provided by the SOHO/SWAN Science Team, in particular within the framework of Research Teams and Working Groups fostered by International Space Science Institute (ISSI), Bern, Switzerland. SWAN, big thank you for sharing your experience with us! The implementation of the GLOWS experiment within the framework of the NASA IMAP mission is based on Agreement between NASA and Poland's Minister of Education and Science. Scientific collaboration between CBK PAN and Physikalisch-Technische Bundesanstalt (PTB) is gratefully acknowledged.

Funding Information GLOWS is funded from Poland's national budget under contract MEiN/2021/2/DIR. Technical development of GLOWS profited from some results of the project FNP TEAM TECH POIR.04.04.00-00-5C65/17-00. Contribution from WAT was supported by Laserlab Europe project (Grant Agreement ID: 871124) and Individual Research Grant UGB 22/773 from WAT for M. Wardzińska. GLOWS-related work in the US was funded by the IMAP mission as a part of NASA's Solar Terrestrial Probes (STP) Program (grant No. 80GSFC19C0027).

Declarations

Competing Interests The authors have no conflicts of interest to declare that are relevant to the content of this article.

References

Baliukin II, Bertaux J-L, Quémerais E, Izmodenov VV, Schmidt W (2019) SWAN/SOHO Lyman-α mapping: the hydrogen geocorona extends well beyond the moon. J Geophys Res 124:861–885. https://doi.org/10.1029/2018JA026136

Baliukin I, Bertaux JL, Bzowski M, Izmodenov V, Lallement T, Provornikova E, Quémerais E (2022) Backscattered solar Lyman-α emission as a tool for the heliospheric boundary exploration. Space Sci Rev 218:45. https://doi.org/10.1007/s11214-022-00913-3. arXiv:2206.15175 [astro-ph.SR]

Barciński T, Kosturek R, Kowalski T, Bzowski M, Wawrzaszek R, Mostowy K, et al (2024) The effect of the coating process thermal cycle on mechanical properties of AA6061-T6 used for load-carrying elements of a space instrument: a case study. Bull Pol Acad Sci 72(5):e150338. https://doi.org/10.24425/bpasts.2024.150338

Bertaux JL, Kyrölä E, Quémerais E, Pellinen R, Lallement R, Schmidt W, et al (1995) SWAN: a study of solar wind anisotropies on SOHO with Lyman Alpha sky mapping. Sol Phys 162(1–2):403–439. https://doi.org/10.1007/BF00733435

Bertaux JL, Lallement R, Quémerais E (1996) UV studies and the solar wind. Space Sci Rev 78:317–328. https://doi.org/10.1007/BF00170818

Bertaux J-L, Quémerais E, Lallement R, Lamassoure E, Schmidt W, Kyrölä E (2000) Monitoring solar activity on the far side of the Sun from sky reflected Lyman α radiation. Geophys Res Lett 27:1331–1334. https://doi.org/10.1029/1999GL003722

Bohlin RC (1996) Spectrophotometric standards from the far-UV to the near-IR of the white dwarf flux scale. Astron J 111(4):1743–1747

Brasken M, Kyrola E (1998) Resonance scattering of Lyman alpha from interstellar hydrogen. Astron Astrophys 332:732–738

Broadfoot AL (1976) Ultraviolet spectrometry of the inner Solar System from Mariner 10. Rev Geophys Space Phys 14:625–627. https://doi.org/10.1029/RG014i004p00625

Broadfoot AL, Kumar S (1978) The interstellar wind: Mariner 10 measurements of hydrogen (1216 Å) and helium (584 Å) interplanetary emission. Astrophys J 222:1054–1067. https://doi.org/10.1086/156223

Bzowski M (2003) Response of the groove in heliospheric Lyman-α glow to latitude-dependent ionization rate. Astron Astrophys 408:1155–1164. https://doi.org/10.1051/0004-6361:20031023

Bzowski M (2008) Survival probability and energy modification of hydrogen Energetic Neutral Atoms on their way from the termination shock to Earth orbit. Astron Astrophys 488:1057–1068. https://doi.org/10.1051/0004-6361:200809393

Bzowski M, Fahr HJ, Ruciński D, Scherer H (1997) Variation of bulk velocity and temperature anisotropy of neutral heliospheric hydrogen during the solar cycle. Astron Astrophys 326:396–411

Bzowski M, Mäkinen T, Kyrölä E, Summanen T, Quèmerais E (2003) Latitudinal structure and North-south asymmetry of the solar wind from Lyman-α remote sensing by SWAN. Astron Astrophys 408:1165–1177. https://doi.org/10.1051/0004-6361:20031022

Bzowski M, Sokół JM, Tokumaru M, Fujiki K, Quémerais E, Lallement R, et al (2013) Solar parameters for modeling the interplanetary background. In: Quémerais E, Snow M, Bonnet R (eds) Cross-calibration of far UV spectra of solar objects and the heliosphere. Springer, Berlin, pp 67–138. https://doi.org/10.1007/978-1-4614-6384-9_3

Bzowski M, Kubiak MA, Strumik M, Kowalska-Leszczynska I, Porowski C, Quémerais E (2023) The flow direction of interstellar neutral H from SOHO/SWAN. Astrophys J 952:2. https://doi.org/10.3847/1538-4357/acda8c. arXiv:2306.01135 [astro-ph.SR]

Christian, et al (2025) The High-energy Ion telescope (HIT) (for the Interstellar Mapping and Acceleration Probe (IMAP) mission. Space Sci Rev

Fahr HJ (1974) The extraterrestrial UV-background and the nearby interstellar medium. Space Sci Rev 15:483–540. https://doi.org/10.1007/BF00178217

Funsten HO, Harper RW, Dors EE, Janzen PA, Larsen BA, MacDonald EA, et al (2015) Comparative response of microchannel plate and channel electron multiplier detectors to penetrating radiation in space. IEEE Trans Nucl Sci 62(5):2283–2293. https://doi.org/10.1109/TNS.2015.2464174

Funsten, et al (2025) The Interstellar Mapping And Acceleration Probe High Energy. (IMAP-Hi) neutral atom imager

Gkioulidou, et al (2025) The IMAP-Ultra energetic neutral atom (ENA) imager

Gruntman M, Roelof EC, Mitchell DG, Fahr HJ, Funsten HO, McComas DJ (2001) Energetic neutral atom imaging of the heliospheric boundary region. J Geophys Res 106:15767–15782. https://doi.org/10.1029/2000JA000328

Hartogh P, Barabash S, Beaudin G, Börner P, Bockeleé-Morvan D, Boogaerts W, et al (2013) The submillimetre wave instrument on JUICE. European planetary science congress (p. EPSC2013-710)

Heerikhuisen J, Pogorelov NV, Zank GP, Crew GB, Frisch PC, Funsten HO, et al (2010) Pick-up ions in the outer heliosheath: a possible mechanism for the interstellar boundary EXplorer ribbon. Astrophys J Lett 708:L126–L130. https://doi.org/10.1088/2041-8205/708/2/L126

Hord CW, Barth CA, Esposito LW, McClintock WE, Pryor WR, Simmons KE, et al (1991) Galileo ultraviolet spectrometer experiment: initial Venus and interplanetary cruise results. Science 253(5027):1548–1550. https://doi.org/10.1126/science.253.5027.1548

Hord CW, McClintock WE, Stewart AIF, Barth CA, Esposito LW, Thomas GE, et al (1992) Galileo ultraviolet spectrometer experiment. Space Sci Rev 60(1–4):503–530. https://doi.org/10.1007/BF00216866

Katushkina OA, Izmodenov VV, Quémerais E, Sokół JM (2013) Heliolatitudinal and time variations of the solar wind mass flux: inferences from the backscattered solar Lyman-alpha intensity maps. J Geophys Res 118:1–9. https://doi.org/10.1002/jgra.50303

Kaźmierczak P, Strumik M, Wawrzaszek R (2021) Baffle design process (Tech. Rep. No. GLOWSBaffleReport:v5.0). Warsaw, Poland: GLOWS Science Team, CBK PAN. Internal memo GLOWS-CBK-RP-2020-11-10-033-v4.0

King JH, Papitashvili NE (2005) Solar wind spatial scales in and comparisons of hourly wind and ACE plasma and magnetic field data. J Geophys Res 110(A9):2104–2111. https://doi.org/10.1029/2004JA010649

Koutroumpa D, Quémerais E, Ferron S, Schmidt W (2019) Global distribution of the solar wind flux and velocity from SOHO/SWAN during SC-23 and SC-24. Geophys Res Lett 46(8):4114–4121. https://doi.org/10.1029/2019GL082402

Kowalski T (2020) Collimator design report (Tech. Rep. No. GLOWS-CBK-TN-2020-12-07-037-v1.0). Warsaw, Poland: GLOWS Science Team, CBK PAN

Krucker S, Hurford GJ, Grimm O, Kögl S, Gröbelbauer HP, Etesi L, et al (2020) The Spectrometer/Telescope for Imaging X-rays (STIX). Astron Astrophys 642:A15. https://doi.org/10.1051/0004-6361/201937362

Kubiak MA, Bzowski M, Kowalska-Leszczynska I, Strumik M (2021a) WawHelioGlow: a model of the heliospheric backscatter glow. II. The helioglow buildup and the potential significance of the anisotropy in the solar EUV output. Astrophys J Suppl Ser 254:17. https://doi.org/10.3847/1538-4365/abeb78. arXiv:2103.02797 [astro-ph.SR]

Kubiak MA, Bzowski M, Kowalska-Leszczynska I, Strumik M (2021b) WawHelioGlow: a model of the heliospheric backscatter glow. I. Model definition. Astrophys J Suppl Ser 254:16. https://doi.org/10.3847/1538-4365/abeb79. arXiv:2103.02802 [astro-ph.SR]

Lallement R, Ferlet R, Lagrange RM, Lemoine M, Vidal-Madjar A (1995) Local cloud structure from HST-GHRS. Astron Astrophys 304:461–474

Lallement R, Quémerais E, Lamy P, Bertaux J-L, Ferron S, Schmidt W (2010) The solar wind as seen by SOHO/SWAN since 1996: comparison with SOHO/LASCO C2 coronal densities. In: Cranmer SR, Hoeksema JT, Kohl JL (eds) SOHO-23: understanding a peculiar solar minimum, ASP Conference Series vol 428. Astronomical Society of the Pacific, San Francisco, pp 253–258

Le Chat G, Issautier K, Meyer-Vernet N (2012) The solar wind energy flux. Sol Phys 279:197–205. https://doi.org/10.1007/s11207-012-9967-y

McComas DJ, Allegrini F, Baldonado J, Blake B, Brandt PC, Burch J, et al (2009a) The Two Wide-angle Imaging Neutral-atom Spectrometers (TWINS) NASA mission-of-opportunity. Space Sci Rev 142(1–4):157–231. https://doi.org/10.1007/s11214-008-9467-4

McComas DJ, Allegrini F, Bochsler P, Bzowski M, Christian ER, Crew GB, et al (2009b) Global observations of the interstellar interaction from the Interstellar Boundary Explorer (IBEX). Science 326:959–962. https://doi.org/10.1126/science.1180906

McComas DJ, Allegrini F, Bochsler P, Bzowski M, Collier M, Fahr H, et al (2009c) IBEX – Interstellar Boundary Explorer. Space Sci Rev 146:11–33. https://doi.org/10.1007/s11214-009-9499-4

McComas DJ, Dayeh MA, Allegrini F, Bzowski M, DeMajistre R, Fujiki K, et al (2012) The first three years of IBEX observations and our evolving heliosphere. Astrophys J Suppl Ser 203:1. https://doi.org/10.1088/0067-0049/203/1/1

McComas DJ, Zirnstein EJ, Bzowski M, Dayeh MA, Funsten HO, Fuselier SA, et al (2017) Seven years of imaging the global heliosphere with IBEX. Astrophys J Suppl Ser 229(2):41. https://doi.org/10.3847/1538-4365/aa66d8

McComas, et al (2025) Interstellar Mapping And Acceleration Probe: the NASA IMAP mission. Space Sci Rev. https://doi.org/10.1007/s11214-025-01224-z

Nass HU, Zoennchen JH, Lay G, Fahr H-J (2006) The TWINS-LAD mission: observations of terrestrial Lyman-α fluxes. Astrophys Space Sci Trans 2:27–31. https://doi.org/10.5194/astra-2-27-2006

Nass H, Zönnchen J, Fahr H (2014) Modellierung der Wasserstoff-Geokorona mit Hilfe von TWINS 1/2 Lyman-α Daten (Tech. Rep. No. GLOWS-CBK-RP-2021-01-15-048-v1.0). Schlussbericht, Argelander Institut für Astronomie, Abt. Astrophysik, Universität Bonn. Report to Bundesministerium für Bildung und Forschung, unpublished

Porowski C, Bzowski M (2024) WawHelioIonMP: a semiempirical tool for the determination of latitudinal variation in the ionization rate of interstellar hydrogen and the solar wind. Astrophys J 967:57. https://doi.org/10.3847/1538-4357/ad3c3d

Porowski C, Bzowski M, Tokumaru M (2022) A new 3D solar wind speed and density model based on interplanetary scintillation. Astrophys J Suppl Ser 259:2. https://doi.org/10.3847/1538-4365/ac35d7. arXiv:2110.15847 [astro-ph.SR]

Porowski C, Bzowski M, Tokumaru M (2023) On the general correlation between 3D solar wind speed and density model and solar proxies. Astrophys J Suppl Ser 264:11. https://doi.org/10.3847/1538-4365/ac9fd4. arXiv:2211.06395 [astro-ph.SR]

Pryor WR, Ajello JM, Barth CA, Hord CW, Stewart AIF, Simmons KE, et al (1992) The GALILEO and PIONEER VENUS ultraviolet spectrometer experiments: solar Lyman-α latitude variation at solar maximum from interplanetary Lyman-α observations. Astrophys J 394:363–377. https://doi.org/10.1086/171589

Pryor WR, Ajello JM, Barth CA, Hord CW, Stewart AIF, Simmons KE, et al (1996) Latitude variations in interplanetary Lyman-a data from the Galileo euvs modeled with solar he 1083 nm images. Geophys Res Lett 23:1893–1896. https://doi.org/10.1029/96GL01978

Pryor WR, Ajello JM, McComas DJ, Witte M, Tobiska WK (2003) Hydrogen atom lifetimes in the three-dimensional heliosphere over the solar cycle. J Geophys Res 108:8034. https://doi.org/10.1029/2003JA009878

Quémerais E, Bertaux J-L (2002a) 14-day forecast of solar indices using interplanetary Lyman α background data. Geophys Res Lett 29(2):1018. https://doi.org/10.1029/2001GL013920

Quemerais E, Bertaux JL (2002b) Radiometric calibration of the SWAN instrument. In: Pauluhn A, von Huber MCE, Steiger R (eds) The radiometric calibration of SOHO. ISSI scientific report series, vol 2, pp 203–210

Quémerais E, Sandel B, Izmodenov V, Gladstone S (2013) Thirty years of interplanetary background data: a global view. In: Quémerais E, Snow M, Bonnet R (eds) Cross-calibration of far UV spectra of solar objects and the heliosphere. ISSI Scientific Report Series, vol 13. Springer, Berlin, pp 141–162. https://doi.org/10.1007/978-1-4614-6384-9_4

Rankin, et al (2025) Solar Wind and Pickup ION (SWAPI) instrument on NASA's Interstellar Mapping And Acceleration Probe

Reisenfeld (2025) Exploring the outer heliosphere through ENA observations from IMAP. Space Sci Rev

Reisenfeld DB, Bzowski M, Funsten HO, Fuselier SA, Galli A, Janzen PH, et al (2016) Tracking the solar cycle through IBEX observations of energetic neutral atom flux variations at the heliospheric poles. Astrophys J 833:277. https://doi.org/10.3847/1538-4357/833/2/277

Reisenfeld DB, Bzowski M, Funsten HO, Janzen PH, Karna N, Kubiak MA, et al (2019) The infuence of polar coronal holes on the polar ENA flux observed by IBEX. Astrophys J 879:1. https://doi.org/10.3847/1538-4357/ab22c0

Reisenfeld DB, Bzowski M, Funsten H, Heerikhuisen J, Janzen P, Kubiak M, et al (2021) A three-dimensional map of the heliosphere from IBEX. Astrophys J Suppl Ser 254:40. https://doi.org/10.3847/1538-4365/abf658

Schwadron, et al (2025). The IMAP-Lo instrument

Skoug, et al (2025) The Solar Wind Electron (SWE) instrument for the Interstellar Mapping and Acceleration Probe mission. Space Sci Rev

Snow M, McClintock WE, Woods TN, White OR, Harder JW, Rottman G (2005) The Mg II index from SORCE. Sol Phys 230:325–344. https://doi.org/10.1007/s11207-005-6879-0

Snow M, Reberac A, Quémerais E, Clarke J, McClintock WE, Woods TN (2013) A new catalog of ultraviolet stellar spectra for calibration. In: Quémerais E, Snow M, Bonnet R-M (eds) Cross-calibration of far UV spectra of solar system objects and the heliosphere. ISSI Scientific Report Series, vol 13. Springer, New York, pp 191–226. https://doi.org/10.1007/978-1-4614-6384-9_7

Sokół JM, Bzowski M (2014) Photoionization rates for helium: update. arXiv e-prints, arXiv:1411.4826. https://doi.org/10.48550/arXiv.1411.4826

Sokół JM, Bzowski M, Tokumaru M, Fujiki K, McComas DJ (2013) Heliolatitude and time variations of solar wind structure from in-situ measurements and interplanetary scintillation observations. Sol Phys 285:167–200. https://doi.org/10.1007/s11207-012-9993-9

Sokół JM, Kubiak MA, Bzowski M, Swaczyna P (2015) Interstellar neutral helium in the heliosphere from IBEX observations. II. The Warsaw Test Particle Model (WTPM). Astrophys J Suppl Ser 220:27. https://doi.org/10.1088/0067-0049/220/2/27. arXiv:1510.04869 [astro-ph.SR]

Sokół JM, McComas DJ, Bzowski M, Tokumaru M (2020) Sun-heliosphere observation-based ionization rates model. Astrophys J 897:179. https://doi.org/10.3847/1538-4357/ab99a4. arXiv:2003.09292 [physics.space-ph]

Strumik M, Bzowski M, Kowalska-Leszczynska I, Kubiak MA (2020) Inferring contributions from unresolved point sources to diffuse emissions measured in UV sky surveys: general method and SOHO/SWAN case study. Astrophys J 899(1):48. https://doi.org/10.3847/1538-4357/ab9e6f. arXiv:2006.12262 [astro-ph.SR]

Strumik M, Bzowski M, Kubiak MA (2021) Influence of heliolatitudinal anisotropy of solar FUV/EUV emissions on lyα helioglow: SOHO/SWAN observations and WawHelioGlow modeling. Astrophys J Lett 919(2):L18. https://doi.org/10.3847/2041-8213/ac2734. arXiv:2109.08095 [astro-ph.SR]

Strumik M, Bzowski M, Kubiak MA (2024a) Effects of heliolatitudinal anisotropy of solar far-ultraviolet/extreme-ultraviolet emissions on Lyα helioglow. Astrophys J 962(1):45. https://doi.org/10.3847/1538-4357/ad1884. arXiv:2312.14039 [astro-ph.SR]

Strumik M, Wardzińska M, Bzowski M, Wachulak P, Wawrzaszek R, Fok T, et al (2024b) Reflectance properties of the acktar magic black^{TM} coating for the radiation near the Lyman-α line of hydrogen: measurements and phenomenological model of the BRDF. J Astron Telesc Instrum Syst 10(1):018004. https://doi.org/10.1117/1.JATIS.10.1.018004

Swaczyna P, Bzowski M, Kubiak MA (2025) Production and loss processes of hydrogen energetic neutral atoms in the heliosphere from 5 ev–500 keV. Astrophys J Suppl Ser 277(1):17. https://doi.org/10.3847/1538-4365/adaf17. arXiv:2411.13174 [physics.space-ph]

Tapping KF (2013) The 10.7 cm solar radio flux ($F_{10.7}$). Space Weather 11:1–13. https://doi.org/10.1002/swe.20064

Tarnopolski S, Bzowski M (2009) Neutral interstellar hydrogen in the inner heliosphere under the influence of wavelength-dependent solar radiation pressure. Astron Astrophys 493:207–216. https://doi.org/10.1051/0004-6361:20077058. arXiv:astro-ph/0701133

Wenger M, Ochsenbein F, Egret D, Dubois P, Bonnarel F, Borde S, et al (2000) The SIMBAD astronomical database. The CDS reference database for astronomical objects. Astron Astrophys Suppl Ser 143:9–22. https://doi.org/10.1051/aas:2000332. arXiv:astro-ph/0002110 [astro-ph]

Wurz P, Galli A, Bzowski M, Möbius E, Janzen P, Gkioulidou M, et al (2021) Interstellar Mapping and Acceleration Probe IMAP ENA and neutral backgrounds. Tech. Rep. Johns Hopkins Applied Physics Laboratory, Laurel, MD. Internal memo

Authors and Affiliations

Maciej Bzowski[1] · Roman Wawrzaszek[1] · Marek Strumik[1] · Jędrzej Baran[1] · Tomasz Barciński[1] · Kamil Ber[1,2] · Waldemar Bujwan[1] · Maciej Daukszo[1] · Kamil Jasiński[1] · Grzegorz Juchnikowski[1] · Przemyslaw Kazmierczak[1] · Izabela Kowalska-Leszczyńska[1] · Tomasz Kowalski[1] · Marzena Kubiak[1] · Jakub Mądry[1] · Aleksandra Mirońska[1] · Karol Mostowy[1] · Piotr Orleański[1] · Czesław Porowski[1] · Jakub Półtorak[1] · Tomasz Rajkowski[1] · Joanna Rothkaehl[1] · Tomasz Rudnicki[1] · Aliaksandra Shmyk[1] · Adam Sikorski[1] · Michał Turek[1] · Marek Winkler[1] · Katarzyna Wojciechowska[1] · Tomasz Zawistowski[1] · Hans J. Fahr[3] · Uwe Nass[3] · Piotr Osica[4] · Karolina Wielgos[4] · Alexander Gottwald[5] · Hendrik Kaser[5] · Mark Krzyzagorski[5] · Marek Antoniak[6] · Marcin Drobik[6] · Grzegorz Gajoch[6] · Tomasz Martyniak[6] · Rafał Żogała[6] · Andrzej Bartnik[7] · Henryk Fiedorowicz[7] · Tomasz Fok[7] · Mateusz Majszyk[7] · Przemysław Wachulak[7] · Martyna Wardzińska[7] · Łukasz Węgrzyński[7] · Robert Kosturek[8] · Carlos Urdiales[9] · Mark Tapley[9] · Susan Pope[9] · Daniel B. Reisenfeld[10] · Matina Gkioulidou[11] · Nathan A. Schwadron[12] · Eric R. Christian[13] · David J. McComas[14]

✉ M. Bzowski
bzowski@cbk.waw.pl

1 Space Research Centre (CBK PAN), Polish Academy of Sciences, Bartycka 18A, Warsaw, 00-716, Poland

2 Present address: Institute of Microelectronics and Optoelectronics, Warsaw University of Technology, Warsaw, 00-662, Poland

3 Argelander Institut für Astrophysik, Bonn University, auf dem Hügel 71, Bonn, D53121, Germany

4 Spacive Sp. z o.o., Augustówka 36, Warsaw, 02-981, Poland

5 Physikalisch-Technische Bundesanstalt (PTB), Abbestr. 2-12, Berlin, D10587, Germany

6 KPLabs, Bojkowska 37J, Gliwice, 44-100, Poland

7 Institute of Optoelectronics, Military University of Technology (WAT), Warsaw, Poland

8 Faculty of Mechanical Engineering, Military University of Technology (WAT), Warsaw, Poland

9 Southwest Research Institute, San Antonio, TX, USA

10 Los Alamos National Laboratory, Los Alamos, NM, 87545, USA

11 Applied Physics Laboratory, Johns Hopkins University, Laurel MD 20723, USA

12 Space Science Center, University of New Hampshire, Durham, NH 03824, USA

13 NASA Goddard Space Flight Center, Greenbelt, MD, 20771, USA

14 Department of Astrophysical Science, Princeton University, Princeton, NJ, 08544, USA